

# A Vertical Resonance Heating Model for X- or Peanut-Shaped Galactic Bulges

Alice C. Quillen<sup>1</sup>, Ivan Minchev<sup>2</sup>, Sanjib Sharma<sup>3</sup>,  
Yu-Jing Qin<sup>4</sup>, & Paola Di Matteo<sup>5</sup>

<sup>1</sup>*Department of Physics and Astronomy, University of Rochester, Rochester, NY 14627, USA*

<sup>2</sup>*Leibniz-Institut für Astrophysik Potsdam (AIP), An der Sternwarte 16, 14482, Potsdam, Germany*

<sup>3</sup>*Sydney Institute for Astronomy, School of Physics, University of Sydney, NSW 2006, Australia*

<sup>4</sup>*Shanghai Astronomical Observatory, 80 Nandan Road, Shanghai, China*

<sup>5</sup>*Observatoire de Paris-Meudon, GEPI, CNRS UMR 8111, 5 pl. Jules Janssen, Meudon, 92195, France*

3 October 2018

## ABSTRACT

We explore a second order Hamiltonian vertical resonance model for X-shaped or peanut-shaped galactic bulges. The X- or peanut-shape is caused by the 2:1 vertical Lindblad resonance with the bar, with two vertical oscillation periods per orbital period in the bar frame. We examine N-body simulations and find that due to the bar slowing down and disk thickening during bar buckling, the resonance and associated peanut-shape moves outward. The peanut-shape is consistent with the location of the 2:1 vertical resonance, independent of whether the bar buckled or not. We estimate the resonance width from the potential  $m = 4$  Fourier component and find that the resonance is narrow, affecting orbits over a narrow range in the angular momentum distribution,  $dL/L \sim 0.05$ . As the resonance moves outward, stars originally in the mid plane are forced out of the mid plane and into orbits just within the resonance separatrix. The height of the separatrix orbits, estimated from the Hamiltonian model, is approximately consistent with the peanut-shape height. The peanut- or X-shape is comprised of stars in the vicinity of the resonance separatrix. The velocity distributions from the simulations illustrate that low inclination orbits are depleted within resonance. Within resonance, the vertical velocity distribution is broad, consistent with resonant heating caused by the passage of the resonance through the disk. In the Milky Way bulge we relate the azimuthally averaged mid-plane mass density near the vertical resonance to the rotation curve and bar pattern speed. At an estimated vertical resonance galactocentric radius of  $\sim 1.3$  kpc, we confirm a mid-plane density of  $\sim 5 \times 10^8 M_{\odot} \text{kpc}^{-3}$ , consistent with recently estimated mass distributions. We find that the rotation curve, bar pattern speed, 2:1 vertical resonance location, X-shape tips, and mid-plane mass density, are all self-consistent in the Milky Way galaxy bulge.

**Key words:** Galaxy: kinematics and dynamics; (Galaxies:) bulges; Galaxies: kinematics and dynamics

## 1 INTRODUCTION

A bimodal distribution has recently been discovered in the distribution of red clump giants in the Galactic bulge (McWilliam & Zoccali 2010; Nataf et al. 2010). The observed distributions can be explained with a vertical X-shaped structure in the bulge region (Saito et al. 2011; Li & Shen 2012; Gerhard & Martinez-Valpuesta 2012; Ness et al. 2012). Proper motions in the X-shaped bulge imply that the bulge is rotating and exhibits non-circular motion (Poleski et al. 2013; Vasquez et al. 2013). The X-shape is primar-

ily comprised of moderate metallicity stars,  $[\text{Fe}/\text{H}] > -0.5$  (Ness et al. 2012).

X-shaped or boxy/peanut-shaped bulge structures are associated with galactic bars (Bureau et al. 2006; Gardner et al. 2013; Erwin & Debattista 2013) and are due to a buckling instability (Raha et al. 1991; Merritt & Sellwood 1994), orbits associated with vertical resonances (Combes et al. 1990; Pfenniger & Friedli 1991) or resonant trapping into a vertical Lindblad resonance during bar growth (Quillen 2002). Orbits supporting the X-shape in N-body simulations are near banana-shaped periodic orbits (Combes et al. 1990; Pfenniger & Friedli 1991; Patsis 2002; Martinez-Valpuesta et al.

2006). Three dimensional N-body simulations with galactic bars exhibit X- or boxy/peanut-shaped bulges (Combes et al. 1990; Raha et al. 1991; Athanassoula 2005; Debattista et al. 2005; Martinez-Valpuesta et al. 2006; Li & Shen 2012; Gardner et al. 2013) and these have been used to model observed boxy/peanut-shaped bulges in galaxies and their velocity distributions, as seen from line widths (Bureau et al. 2006; Mendez-Abreu et al. 2008; Gardner et al. 2013).

Because resonances are often narrow, their location is strongly dependent on the calculated values of rotation and oscillation periods. For example, a resonant model has placed tight constraints on the Milky Way's bar pattern speed (Minchev et al. 2007; Gardner & Flynn 2010,b). If the X-shape in our Galaxy is related to a vertical Lindblad resonance, then its location gives a tight relation between the bar pattern speed, the angular rotation rate and the vertical oscillation frequency. This can give a potentially important constraint on the mass distribution in the inner region of our Galaxy. Furthermore if the resonance has drifted, then it may be possible to also place constraints on the past evolution of the Milky Way's bar and bulge by identifying its affect on the velocity distributions.

In this paper we expand on the Hamiltonian resonant model for the dynamics near a vertical resonance by Quillen (2002). This model provides a theoretical framework for predicting the location and inclinations of orbits in the vicinity of the resonance. We compare predictions made with this model to numerical simulations of barred galaxies that exhibit peanut shaped bulges. We test the assumption that the X-shape bulge in the Milky Way is associated with a vertical resonance by comparing the mid-plane mass density predicted from a vertical resonance model to that inferred from observations.

## 2 HAMILTONIAN MODEL FOR A VERTICAL RESONANCE

Orbital dynamics in a galaxy can be modeled with an axisymmetric Hamiltonian with the addition of perturbations from non-axisymmetric structures such as a bar (e.g., Contopoulos 1975). The family of banana-shaped periodic orbits have two vertical oscillations per rotation period in the frame rotating with the bar (Combes et al. 1990; Pfenniger & Friedli 1991; Patsis 2002). At this commensurability,

$$\nu \approx 2(\Omega - \Omega_b), \quad (1)$$

where  $\Omega$  is the angular rotation rate in the plane,  $\nu$  the frequency of vertical oscillations (both at a mean or guiding orbital radius,  $r_g$ ), and  $\Omega_b$  is the bar pattern angular rotation rate. The above commensurability is also known as a vertical Lindblad resonance and its role in accounting for boxy peanut shaped bulges was suggested by Combes et al. (1990). In the bar frame there are two vertical oscillation periods per rotation period. The resonance is often called a 2:1 vertical Lindblad resonance. By integrating the above expression we find a resonant angle or resonant argument

$$\phi \equiv \theta_z + 2(\theta - \Omega_b t) \quad (2)$$

that is slowly moving near the resonance. Here  $\theta_z$  is the angle associated with vertical oscillations and  $\theta$  the azimuthal

angle in the galactic plane. The periodic banana-shaped periodic orbits have constant values of resonant angle  $\phi = 0$  or  $\pi$ . The value of the constant value specifies the orientation of the periodic orbit (banana pointed up or banana pointed down). When the angle  $\phi$  is fixed, variations in  $\theta$  are related to variations in  $\theta_z$ , however no epicyclic or radial oscillation is specified. By considering a single dimension of freedom, the vertical one, we have ignored the radial degree of freedom. We refer to constant  $\phi$  orbits as periodic orbits, however, they would only be periodic in three dimensions if they were also periodic in their radial degree of freedom. When the orbit is periodic in three dimensions and reaches apocenter when at high inclination above or below the mid-plane, then the orbit is banana-shaped.

Near a resonance, only perturbative terms to the Hamiltonian that contain slowly varying angles need be considered. Those with rapidly varying angles only cause small perturbations to action variables and so can be neglected. Following Quillen (2002), the dynamics near a vertical Lindblad resonance can be modeled with a Hamiltonian

$$H(J_z, \phi) = aJ_z^2 + \delta J_z + \epsilon_s J_z \cos(2\phi) \quad (3)$$

in a galaxy that is symmetrical about the mid plane. Here  $J_z$  is the action variable associated with vertical oscillations that is conjugate to the angle  $\theta_z$ . At low inclination, action angle variables,  $J_z, \theta_z$ , are related to positions and velocities in cylindrical coordinates

$$\begin{aligned} z &\approx \sqrt{\frac{2J_z}{\nu}} \cos \theta_z \\ v_z &\approx -\sqrt{2J_z\nu} \sin \theta_z \\ \theta_z &= \nu t + \text{constant}, \end{aligned} \quad (4)$$

where  $z$  is the height above the Galactic plane and  $v_z$  the vertical velocity component. The coefficient  $a$  depends only on the symmetric mass distribution in the galaxy. The first two terms in the Hamiltonian (equation 3) arise from the unperturbed system alone or the axisymmetric gravitational potential. The coefficient  $\epsilon_s$  depends on the bar perturbation strength and shape. The coefficients  $a, \delta$  depend on angular momentum (or mean radius) and are derived more rigorously in our appendices A and B, expanding on the calculations by Quillen (2002).

The coefficient  $\delta$  describes distance from resonance,

$$\delta \approx \nu - 2(\Omega - \Omega_b). \quad (5)$$

The vertical oscillation frequency,  $\nu$ , depends on the axisymmetric (or azimuthally averaged) mass distribution with

$$\nu^2 \equiv \left. \frac{\partial^2 V_0}{\partial z^2} \right|_{z=0} \quad (6)$$

evaluated in mid-plane at approximately the mean radius  $r_g$  of the orbit (see appendix A for description in terms of angular momentum and all three action angle variables). Here  $V_0(r, z)$  is the gravitational potential derived from the axisymmetric mass distribution. The above one dimensional Hamiltonian depends not on  $J_z, \theta_z$  but on  $J_z, \phi$ . Canonical transformations reduce the full three dimensional Hamiltonian to the one dimensional version given in above equation 3 and this is shown in appendix B.

As the orbit transverses different radii, the star crosses regions with different values of  $\frac{\partial^2 V_0}{\partial z^2}$ . This sensitivity is taken

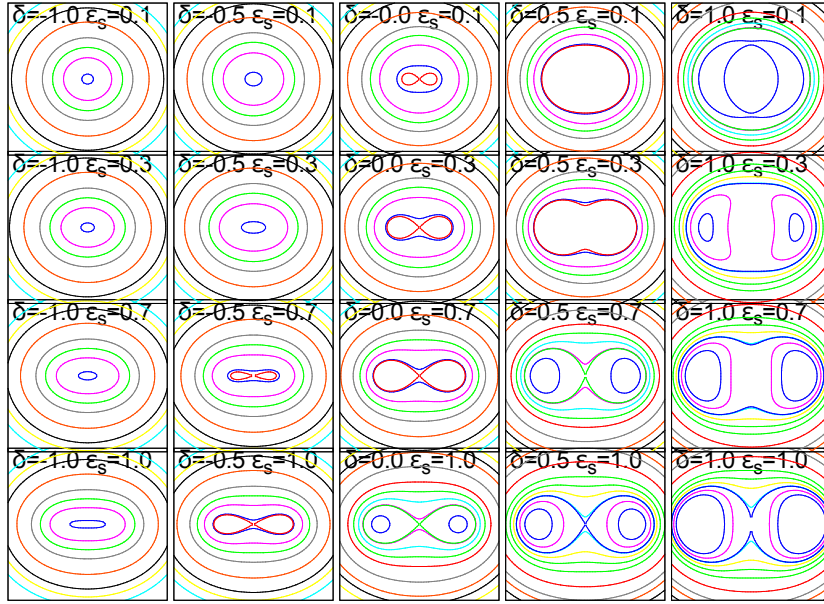


**Figure 1.** Level curves are shown for the Hamiltonian in equation 3 showing bar growth. Level curves of the second order Hamiltonian in equation 3 are shown to illustrate classes of periodic orbits for different values of  $\delta$  or distance to resonance. The level curves are shown in a coordinate system with  $(x, y) = \sqrt{2J_z}(\cos \phi, \sin \phi)$ , so radius on the plot is equal to  $\sqrt{2J_z}$ . Higher radius in each panel corresponds to higher orbital inclination. Fixed points correspond to orbits that are periodic in  $\phi_z$  and  $\theta$ . The stable periodic orbits are found at  $\phi = 0, \pi$  and these correspond to upward oriented banana-shaped orbits and downward oriented banana shaped orbits. The banana-shaped orbits reach high inclination along the bar major axis and lie slightly below the mid-plane along the bar minor axis. On resonance there are no planar orbits. If the product of coefficients  $a\epsilon_s$  is positive rather than negative, then each panel is rotated by  $90^\circ$  and the orbits are below the mid-plane at the ends of the bar and reach high inclinations along the bar minor axis. From top to bottom each row is meant to represent a different time. From left to right each panel shows a different radial location in the galaxy from small radius (left, low  $\delta$ ) to larger radius (right higher  $\delta$ ). Bar growth is shown with increasing perturbation strength  $\epsilon_s$  from top to bottom.

into account with Hamiltonian terms that depend on both  $J_z$  and  $J_r$ , the action variable associated with epicyclic motion (see appendix A). A term proportional to  $J_r J_z$  can introduce a small shift in the location of resonance (see appendix C), here described by the coefficient  $\delta$ .

The bar gravitational potential perturbation's vertical dependence,  $V_b(r, \theta, z, t)$ , can be approximated to low order in  $z$  with a sum of Fourier components

$$V_m(r, \theta, z, t) = [C_m(r) + C_{mz}(r)z^2] \cos(m(\theta - \Omega_b t)). \quad (7)$$

Each  $m$  is a Fourier component of the bar's gravitational potential and we have retained the dependence on  $z$ . Above it is assumed that the gravitational potential is symmetric about the mid-plane and that when the bar grows only the Fourier amplitudes, described by the coefficients,  $C_m, C_{mz}$ , increase in strength. Here  $C_m$  has units of gravitational potential,  $(\text{km/s})^2$ , and  $C_{mz}$  has units  $(\text{km/s})^2 \text{ kpc}^{-2}$  or  $\text{frequency}^2$ . For a bar that is similar shape on either side of the mid-plane (buckle-free), we need only consider  $m = 2$  and 4 Fourier components. The  $m = 4$  term contributes to the 2:1 resonance associated with banana-shaped orbits and with resonant angle given in equation 2. Inserting the expression for  $z$  (equation 4) into the above potential expression we can write the potential term that is proportional to  $z^2$  in terms of action variables as

$$\frac{C_{mz}}{4} \left( \frac{2J_z}{\nu} \right) [\cos(2\theta_z - m(\theta - \Omega_b t)) + \cos(2\theta_z + m(\theta - \Omega_b t))] \quad (8)$$

where the first term is important near an inner  $m:1$  vertical resonance and the second term is appropriate for an outer vertical resonance. Henceforth we neglect the outer resonance term. For  $m = 4$  the resonant angle is equivalent to  $2\phi$  as defined in equation 2 and we find the coefficient in equation 3,

$$\epsilon_s = \frac{C_{4z}}{2\nu}. \quad (9)$$

This coefficient has units of frequency.

If the bar buckles during growth we can also consider a time dependent perturbation that includes an asymmetric term

$$V_2(r, \theta, z, t) = B_{2z}(r, t)z \cos(2(\theta - \Omega_b t)). \quad (10)$$

Inserting  $z$  in action angle variables we find a perturbation term in the form

$$\frac{B_{2z}}{2} \sqrt{\frac{2J_z}{\nu}} [\cos(\theta_z - 2(\theta - \Omega_b t)) + \cos(\theta_z - 2(\theta - \Omega_b t))] \quad (11)$$

In this case we would consider a Hamiltonian

$$H(J_z, \phi) = aJ_z^2 + \delta J_z + \epsilon_b J_z^{1/2} \cos(\phi) \quad (12)$$

with

$$\epsilon_b = \frac{B_{2z}}{\sqrt{2\nu}}. \quad (13)$$

While the Hamiltonian given in equation 3 is equivalent to a second order mean motion resonance, that given in equa-

tion 12 is equivalent to a first order mean motion resonance (see Murray & Dermott 1999 chapter 8). The order refers to the power of  $J_z^{\frac{1}{2}}$  in the perturbation term, corresponding to the power of eccentricity or inclination, depending upon the setting.

When the galaxy is symmetric about the mid plane it may seem mysterious that the 2:1 vertical resonance strength depends on the  $m = 4$  Fourier coefficient of the gravitational potential. We can consider the morphology of the banana-shaped orbit in a frame moving with the bar. It is high above the mid plane at the ends of the bar, on the bar major axis, and below the mid plane on the bar minor axis. Because the gravitational potential is symmetrical about the mid plane, the orbit reaches high points in the potential both along the major axis and along the minor axis. Thus a star in the orbit experiences positive extrema in the potential at four points in the orbit. Consequently the  $m = 4$  perturbation associated with the bar excites the 2:1 vertical resonance.

We can qualitatively consider the coupling when the galaxy is buckling. Because of the buckle the potential is low along the bar major axis and high along the bar minor axis. For an orbit oriented with the buckle, the  $m = 2$  Fourier component from the bar perturbation excites the resonance.

## 2.1 Resonance size scales

The coefficient  $\delta$  describes the distance from resonance and so can be ignored when considering the characteristic momentum and timescale in resonance. These size scales can be estimated from the coefficients  $a, \epsilon_s$  or from  $a, \epsilon_b$  (see Quillen 2006 equation 7). For a first order resonance, the important timescale,  $\tau_{lib}$  (a libration timescale), and momentum scale,  $J_{res}$ ,

$$\begin{aligned} \tau_{lib} &= \left| \epsilon_b^2 a \right|^{-\frac{1}{3}} \\ J_{res} &= \left| \frac{\epsilon_b}{a} \right|^{\frac{2}{3}}, \end{aligned} \quad (14)$$

and for the second order resonance

$$\begin{aligned} \tau_{lib} &= |\epsilon_s|^{-1} \\ J_{res} &= \left| \frac{\epsilon_s}{a} \right|. \end{aligned} \quad (15)$$

We refer to a libration frequency,  $\omega_{lib} = \tau_{lib}^{-1}$ .

As  $\delta$  is a frequency, we can estimate the width of the resonance by considering where  $\delta$  is similar in size to the libration frequency. At low inclination, the region where the resonance is important is where  $|\delta| \lesssim \tau_{lib}^{-1}$  or

$$|\delta| \lesssim \begin{cases} \left| \frac{\epsilon_b^2 a}{|\epsilon_s|} \right|^{\frac{1}{3}} & \text{for first order} \\ |\epsilon_s| & \text{for second order} \end{cases}, \quad (16)$$

where the first and second expressions correspond to first and second order resonances, respectively. At high inclination, the mean inclination of the orbit contributes to the resonance width. For  $J_z \gtrsim J_{res}$  the libration timescale can be estimated from the frequency of libration in a pendulum model or

$$\tau_{lib} \approx \sqrt{\frac{\epsilon_s J_z}{a}} \quad \text{for second order} \quad (17)$$

$$\approx \sqrt{\frac{\epsilon_b J_z^{1/2}}{a}} \quad \text{for first order} \quad (18)$$

## 2.2 Hamiltonian Level Curves

In Figures 1 and 2 we show level curves of the second order Hamiltonian (equation 3) in a canonical coordinate system with  $(x, y) = \sqrt{2J_z}(\cos \phi, \sin \phi)$  so that radius on the plot scales with orbital inclination or the maximum height of the orbit above the midplane. Panels from left to right show increasing values of  $\delta$  or radius. Convention is given here for  $a < 0, \epsilon_s > 0$  and  $\delta$  defined as in equation 5. In this Figure, labels correspond to  $\delta$  and  $\nu$  normalized so that  $a = -1$ . The frequency setting distance to resonance,  $\delta$ , is expected to increase with increasing radius, and be negative inside resonance and positive outside resonance. As the bar slows down, reducing  $\Omega_b$ , or the disk thickens, reducing the vertical oscillation frequency  $\nu$ , the distance to resonance,  $\delta$ , decreases, moving the resonance outward to larger radius.

On either side of resonance in Figure 1 (left or right panels) corresponding to large positive or large negative  $\delta$ , orbits at the origin remain at low inclination in the mid-plane. In the intermediate regions,  $|\frac{\delta}{\epsilon_s}| < 1$ , there are no planar orbits. Only a single fixed point exists for  $\frac{\delta}{|\epsilon_s|} < -1$ , two stable fixed points exist for  $|\frac{\delta}{\epsilon_s}| < 1$  and three for  $\frac{\delta}{|\epsilon_s|} > 1$ .

Fixed points, corresponding to periodic orbits in  $z, \theta$  and  $\theta_z$  in the bar's corotating frame, can be found by setting Hamilton's equations to zero and solving for their values of  $J_z, \phi$ . The stable fixed points satisfy  $\phi = 0$  or  $\pi$ . In the region where there are two stable fixed points

$$J_{z, fixed}(\delta) = \frac{\delta + \epsilon_s}{(-2a)} \quad \text{for} \quad \left| \frac{\delta}{\epsilon_s} \right| < 1. \quad (19)$$

The fixed points correspond to banana-shaped orbits where the orbit can reach a high inclination at the ends of the bar. Fixed points at  $\phi = 0$  correspond to periodic orbits in the family denoted BAN+, upward facing banana-shaped orbits, and those at  $\phi = \pi$  to BAN-, a downward facing banana-shaped orbit family (e.g., Pfenniger & Friedli 1991; Martinez-Valpuesta et al. 2006). The two periodic orbit families are predicted by the Hamiltonian model but exist over a narrow range in  $\delta$ . At large negative  $\delta$  the only fixed point is low inclination. At large positive  $\delta$  periodic orbits only exist in the mid plane or at extremely high inclinations.

The fixed point value of  $J_z$  ranges from 0 where  $\delta = -|\epsilon_s|$  to  $J_{z, fixed} = \left| \frac{\epsilon_s}{a} \right|$  where  $\delta = |\epsilon_s|$ . The maximum value for the fixed point  $J_{z, fixed}$  (at  $\delta = \epsilon_s$ ), in the region where there are no planar orbits, is equal to the  $J_{res}$  value estimated from dimensional analysis (equation 15). For  $a$  negative and  $\epsilon_s$  positive, fixed points have  $\phi = 0, \pi$ .

In the region  $|\delta/\epsilon_s| < 1$ , where there are no planar orbits, using the Hamiltonian (equation 3) we can write the energy as a function of  $J_{z, fixed}$

$$\begin{aligned} H &= aJ_{z, fixed}^2 + J_{z, fixed}(\delta + \epsilon_s) = 3aJ_{z, fixed}^2 \\ &= \frac{3}{4}a z_f^4 \nu^2 \end{aligned} \quad (20)$$

For the last step we have used the relation between  $z$  and  $J_z$  (equation 4) and denoted  $z_f$  as the maximum height of the periodic orbit with  $J_{z, fixed}$ . This predicts a quadratic

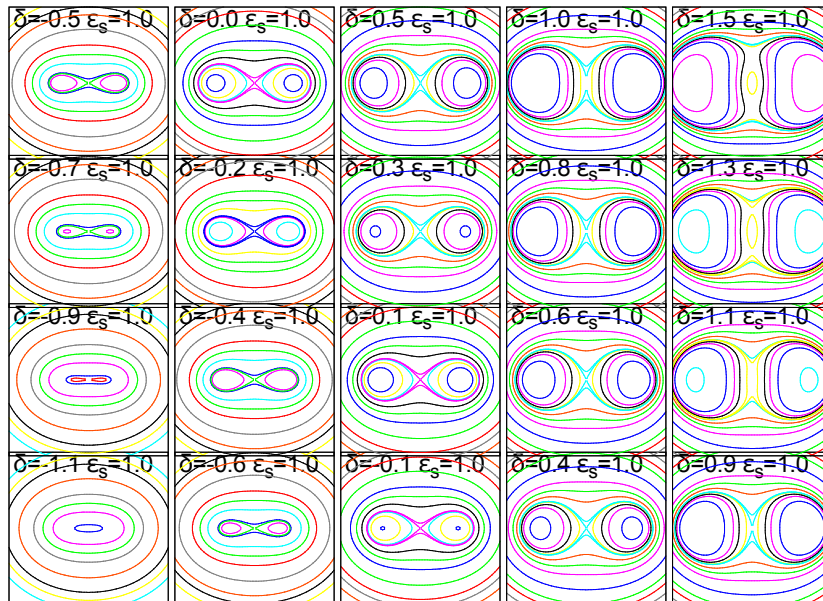


**Figure 2.** Similar to Figure 1 except the bar slows down from top to bottom panels but is kept at the same strength. The evolution is similar if the disk thickens. Both processes decrease  $\delta$  and move the resonance outward in radius. On the rightmost panel, as  $\delta$  decreases the island of low inclination orbits fades away. Stars originally in low inclination orbits in this island at the outer edge of the peanut are pushed out of the plane and into high inclination orbits just inside the separatrix. As the resonance continues to drift (see second column from right) the separatrix shrinks and these stars then must cross the separatrix. Eventually they are left in high inclination orbits that circulate outside resonance and so do not support the peanut shape. Stars are heated vertically as they pass through resonance. While they are just inside the separatrix they librate around  $\phi = 0$  or  $\phi = \pi$  and support the peanut-shape. A signature of adiabatic bar slowing or disk thickening would be a population of stars at the outer edge of resonance, just inside the separatrix, with height  $z_{sep}$  (equation 21).

relation between the heights of the BAN+ and BAN- families as a function of the Jacobi integral of motion. With the addition of terms depending upon the radial degree of freedom, our Hamiltonian is the Jacobi constant (see the appendices A and B). While Pfenniger & Friedli (1991); Martinez-Valpuesta et al. (2006) have plotted the height of the periodic orbits of the BAN+ and BAN- families as a function of Jacobi constant, up to now a functional relation has been lacking. In future the Hamiltonian model could be tested with fits to the bifurcation diagram. The bifurcation diagram could also be predicted for different simulation snapshots taking into account variations in the coefficient  $a$ , the location of the resonance and the resonance strength.

If the product  $a\epsilon_s$  is positive then the level curves are rotated by  $90^\circ$ , and fixed points have  $\phi = \pm\pi/2$ , corresponding to periodic orbits in the ABAN (anti-banana) family (Pfenniger & Friedli 1991). The orbits are near the mid-plane at the ends of the bar and are at high inclination along the bar minor axis. These are figure eight or infinity-shaped when projected on the  $xz$  plane (with the  $x$  axis is oriented on the bar major axis, see Figure 8 by Martinez-Valpuesta et al. 2006) and are usually unstable (Skokos et al. 2002). The product  $a\epsilon_s$  is dependent on radius. It is possible that periodic orbits in the ABAN family could appear in a region where  $a\epsilon_s$  is negative. Fixed points in our low order model lie on a line (so you either have BAN+,BAN- or ABAN but not both) but a higher order model (in  $J_z$ ) could give simultaneously both classes of periodic orbit families.

The Hamiltonian level curves can also be used to explore

when an orbit supports or contributes to a peanut shape in the galaxy. Orbits that have  $\phi$  librating around 0 would spend more time above the plane at the bar ends and less time below the plane there. Those librating about  $\pi$  would spend more time below the plane at the bar ends. These orbits would support a peanut shape as they are coherent with the bar. However orbits that circulate about the origin could not provide good support for a peanut shape. For  $|\delta/\epsilon_s| < 1$  the division between the two classes of orbits occurs on an orbit that contains the unstable fixed point at the origin and is called the separatrix. The separatrix contains two unstable orbits and separates orbits librating around  $\phi = 0$  and  $\pi$  from those circulating about the origin nearer the mid plane. The level curves in Figure 1 illustrate that for  $\delta < -\epsilon_s$  orbits do not support a peanut shape. However, for  $\delta > \epsilon_s$  high inclination islands exist that would support a peanut shape. In between, all orbits within the separatrix and those near the separatrix support the peanut, but those at high inclinations do not.

Also of interest is the separatrix height. Where  $\delta = |\epsilon_s|$  the separatrix consists of two circles that touch at the origin (see right lower panel in Figure 1). The circles have a maximum distance from the origin corresponding to  $J_{z,sep} = |2\epsilon_s/a|$  giving a maximum height in these orbits of

$$z_{sep} = 2 \left| \frac{\epsilon_s}{a\nu} \right|^{1/2} \quad (21)$$

we we have used equation 4 relating  $z$  and  $J_z$ .

### 2.3 Bar growth, bar slowing and disk thickening

Figure 1 illustrates how phase space varies during bar growth, whereas Figure 2 illustrates how phase varies as the bar slows down or the disk thickens. In these figures each column is meant to represent a different radius and each row a different time. From top to bottom in Figure 1 we show variations in the Hamiltonian (equation 3) level curves as the coefficient of bar perturbation strength  $\epsilon_s$  increases. From left to right the coefficient  $\delta$ , controlling distance to resonance, increases. In figure 2 from top to bottom  $\delta$  is slowly decreased to illustrate the effect of bar slowing or disk thickening, with increasing time going from top to bottom.

Recall that volume in phase space is conserved if evolution is adiabatic. Stars originally in the mid-plane would be located at the origin in Figure 1. If bar growth is adiabatic then those stars must remain in a small area or volume. This means that they would remain near the fixed points (corresponding to banana-shaped periodic orbits) in these panels. When the vertical oscillation frequency,  $\nu$ , the coefficient  $a$ , and the bar pattern speed,  $\Omega_b$ , do not vary then  $\delta(r)$  is constant. If the bar grows in strength, then  $\epsilon_s$  increases in time. In this case phase space varies as shown going downward in Figure 1. If the bar strength increases adiabatically, within the region  $|\delta| < |\epsilon_s|$ , stars originally in the mid-plane remain near periodic orbits (fixed points) and are lifted into high inclination orbits and remain near a periodic orbit family (Quillen 2002). For  $|\delta| > |\epsilon_s|$  orbits exist in the mid-plane at all times and so stars originally at low inclination can remain there. The vertical height of the bulge as a function of radius would depend on the height of the periodic orbits (equation 19). The peanut height would be zero where  $\delta = -|\epsilon_s|$  and reach a maximum of

$$z_{max} = \sqrt{\left| \frac{2\epsilon_s}{a\nu} \right|} = \sqrt{\frac{C_{4z}}{a\nu^2}} \quad (22)$$

where  $\delta = |\epsilon_s|$ . Above we have used equation 9 for  $\epsilon_s$ . The height,  $z_{max}$ , is the maximum fixed point height within the region where there are no in-plane or low inclination orbits. There are higher fixed points at larger  $\delta$  but these exist at radii where there are also planar orbits (see panel on upper right in Figure 2).

Quillen (2002) proposed that a bow-tie or X-shape would be seen because of the linear dependence of the fixed point action variable  $J_z$  on the distance to resonance,  $\delta$ . Using expressions for  $\delta, a, \nu, C_{4z}$  as a function of radius, the height of a peanut could approximately be predicted using

$$z(\delta) = z_{max} \frac{1}{2} \left( 1 + \frac{\delta}{\epsilon_s} \right) \quad \text{for} \quad \left| \frac{\delta}{\epsilon_s} \right| < 1, \quad (23)$$

if only  $\epsilon_s$  varies during bar growth and bar growth is adiabatic. This prediction is appropriate if the resonance is wide. In other words, the region spanned by  $|\delta/\epsilon_s| < 1$  must be wide enough to match the extent of observed peanut shapes. As we will show below, the resonance is not wide enough to confirm this expectation.

If the bar growth is not adiabatic then stars originally near fixed points would not be restricted to remain near fixed points or period orbits. If the resonance is thin and weak (corresponding to small  $\epsilon_s$ ), it would have a slow libration frequency, and even slow evolution in the galaxy may not be adiabatic. In this case the distribution of stars is heated by the resonance even during bar growth. In the re-

gion  $|\delta/\epsilon_s| < 1$  there are no orbits in the mid-plane, so stars should have a height distribution at least as large as  $z(\delta)$  following bar growth. Quillen (2002) primarily discussed resonance trapping due to adiabatic bar growth but showed that even when a bar grew moderately quickly, an X-shape was seen in simulated stellar height distributions. The adiabatic limit can be estimated from the square of the libration timescale (Quillen 2006). Hence variations in the coefficients  $\epsilon_s, \delta$  can be considered adiabatic if for example  $|\dot{\epsilon}_s| \lesssim \epsilon_s^2$  or  $|\dot{\delta}| \lesssim \epsilon_s^2$ .

When the bar slows down, or the disk thickens, the parameter  $\delta$  increases. This setting is illustrated in Figure 2 showing level curves with fixed perturbation strength  $\epsilon_s$  but  $\delta$  decreasing from top to bottom panels. As the resonance moves outward, stars originally in the mid plane just outside resonance are forced out of the mid plane and into high inclination orbits. If the evolution is adiabatic, stars originally near fixed points are pushed back into the mid plane. The separatrix shrinks in size (moving downward on the figure). Stars librating about fixed points eventually cross the separatrix. Afterwards their orbits take them around the origin so the angle  $\phi$  oscillates and they no longer support the peanut or X-shape. A star that originally is outside of resonance, and in the mid plane, is first heated to high inclination when it enters resonance, when it must enter an orbit just within the separatrix. Then as the separatrix shrinks the star must leave the resonance, but it will leave at a high inclination. If the resonance continues to drift outward then it will leave high inclination stars behind with angle  $\phi$  circulating rather than librating. The resonance heats the stars to a height approximately equal to the separatrix height (equation 21). The fate of stars originally in the mid plane just exterior to resonance is illustrated in Figure 3 for adiabatic drift. If the drift is not adiabatic then one can think of an instantaneous mapping between panels in Figure 2 rather than continuous evolution of area preserving volumes as shown in Figure 3

The resonance size scale and timescale can be used to estimate how long it takes an orbit to be heated by the resonance. For example, a star placed at the unstable fixed point near the origin would exponentially move away reaching an height of order  $z_{max}$  in a timescale of order  $\tau_{lib}$ .

If the bar speeds up or if gas is accreted adding mass to the mid plane and raising the vertical oscillation frequency, then the resonance moves inward instead of outward. In this case we consider Figure 2 but evolution is upward on this figure instead of downward. Particles trapped near fixed points would be lifted to even higher inclination. In this case an X-shape would also be seen but it would extend to  $\delta > \epsilon_s$ . This situation is similar to the capture of Pluto in resonance with Neptune. If the bar speed increase is adiabatic stars would be confined to high inclination orbits, near fixed points, at a radius where mid plane orbits are allowed.

The role of the disk thickness in influencing the vertical oscillation frequency was a key property of a time dependent resonant trapping model for disk thickening and bulge growth in the absence of a bar by Sridhar & Touma (1996a,b). Here also the resonance itself can cause the disk to thicken, reducing the vertical oscillation frequency  $\nu$  and the perturbation strength  $\epsilon_s$  and possibly decreasing  $a$ . A time dependent Hamiltonian could in future be used to construct an instability model for the growth of the peanut.

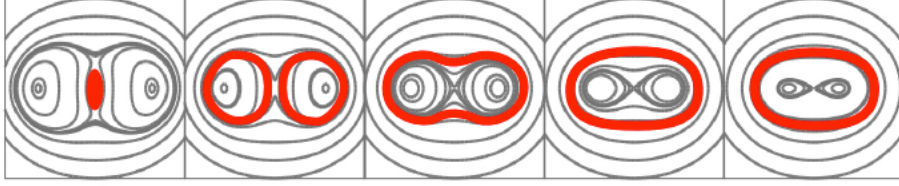


**Figure 3.** Hamiltonian level curves showing the evolution in phase space of stars originally located exterior to the resonance in the mid plane as the resonance drifts outward. In the leftmost panel stars near the origin, in the mid plane, and just outside resonance are in the red area. As the resonance moves outward, (moving from left to right panels) stars are first forced out of the mid plane and into orbits just interior to the separatrix (second panel from left). Inside the separatrix (panel second from left) stars librate about  $\phi = 0$  (right red oval) or  $\pi$  (left red oval) and so support an X-shape. Then as the separatrix shrinks, the stars leave the separatrix and are left at high inclination but no longer support the peanut or X-shape (rightmost two panels). Outside the separatrix (rightmost three panels) the angle  $\phi$  oscillates about the origin. We associate stars in the vicinity of the resonance separatrix, shown in the red area in the second panel on left, and in the middle panel as stars in the X-shape. Stars interior to the separatrix would be banana shaped, either oriented up or down depending upon the value of the nearest periodic orbit. Stars just exterior to the separatrix would have morphology similar to the sum of upward and downward banana-shaped orbits. Because they spend little time near  $\phi = \pm\pi/2$  they would support the peanut shape even though  $\phi$  oscillates instead of librating.

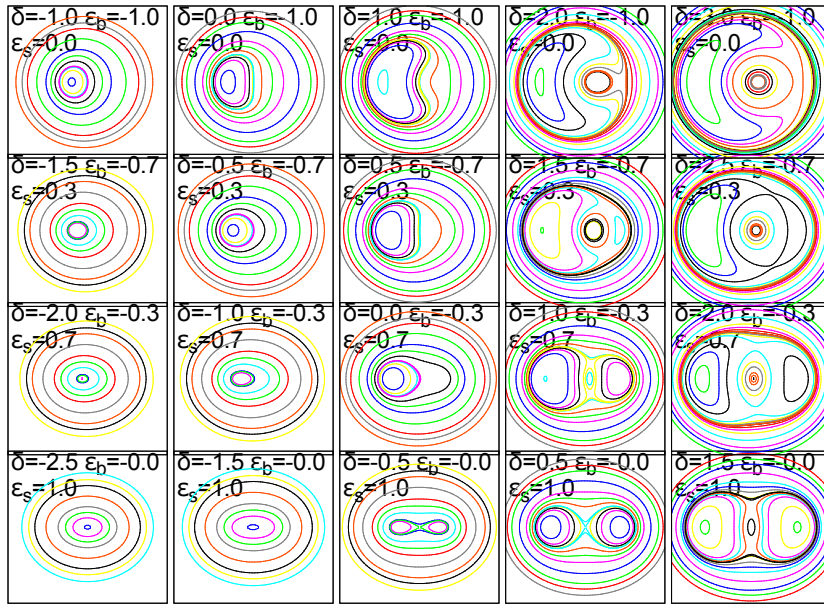


**Figure 4.** Level curves of the Hamiltonian in equation 24 are shown showing the transition between first and second order that would take place following bar buckling. From left to right the coefficient  $\delta$ , setting distance to resonance increases. From top to bottom,  $|\epsilon_b|$  decreases while  $\epsilon_s$  increases. On the bottom periodic orbits giving both upward and downward banana shaped are present ( $\phi = 0$  and  $\phi = \pi$ ). However on the top, orbits supporting the buckling dominate on the outer side of resonance and those pointed opposite are found on the inner side. If the transition is adiabatic then orbits trapped in one family (orbits supporting the bar buckle) could remain at high inclination. Afterward more stars could be found in one family of banana shaped periodic orbits than the other. It is possible that an asymmetry could persist in the phase space distribution after the bar buckled.

#### 2.4 Transition from bar buckling to a symmetric potential

When a bar buckles the Hamiltonian resembles the first order one, equation 12. However as the buckling dies away,  $\epsilon_b$  drops. Weaker second order terms become more important and the Hamiltonian resembles the second order one, equation 3. We can consider a Hamiltonian that contains both first and second order terms or

$$H(J_z, \phi) = aJ_z^2 + \delta J_z + [\epsilon_s J_z + \epsilon_b J_z^{1/2}] \cos 2\phi \quad (24)$$

We expect  $a, \epsilon_b < 0$  and  $\epsilon_s > 0$  (see Figure 13 below showing potential shapes). Level curves for this Hamiltonian are shown in Figure 4 showing the effect of decreasing  $|\epsilon_b|$  and increasing  $\epsilon_s$ . This mimics the transition between bar buckling and a symmetric state. Both first order and second order Hamiltonians have fixed points at  $\phi = 0, \pi$ , corresponding to upwards and downwards facing banana shaped periodic orbits. However, one class has much higher inclination than the other for first order Hamiltonian (top panels in Figure 4) and  $\delta > 0$ . As symmetry about the mid plane is restored, both families of banana shaped periodic orbits are present

and they have similar inclination. If the transition is adiabatic, then one family of banana shaped orbits could be more populated. An asymmetry may persist in the number of stars in each periodic orbit family after bar buckling.

### 3 PEANUT SHAPED BULGE FORMATION IN NUMERICAL SIMULATIONS

To test the resonant model for a peanut-shaped bulge we examine peanut-shaped distributions present in N-body simulations. We study isolated giant disk galaxy simulations denoted ‘gSa’ and ‘gS0’ from the GalMer database (Di Matteo et al. 2007; Chilingarian et al. 2010). The simulations include 320,000 (gS0) or 240,000 (gSa) disk particles, and 160,000 dark matter halo particles. The initial halo and bulge are modeled as Plummer spheres. The initial gaseous and stellar discs follow Miyamoto-Nagai density profiles. The Toomre parameter of both stars and gas is taken to be  $Q = 1.2$  as the initial condition of the Tree-SPH simulations. GalMer simulations outputs have velocities in 100 km/s, positions in kpc, potential in units of  $(100 \text{ km/s})^2$  and timesteps in units of Gyr. For a discussion of the properties of the isolated disk GalMer simulations see Minchev et al. (2012). These simulations were chosen because they have many disk particles and displayed strong bars. In the gS0 simulation the bar buckles, whereas the bar did not buckle in the gSa simulation. A comparison of the two simulations is particularly interesting because of this difference in bar evolution. Both simulations exhibit strong peanut-shaped bulges at later times.

In Figure 5 two snapshots of the stars alone from the gSa simulation are shown, the first one at 1 Gyr, just after bar growth and the second one at 2.74 Gyr, at the end of the simulation. As can be seen from the vertical disk density profiles, the galaxy is strongly peanut-shaped and the peanut shape continues to grow after bar formation. There is no evidence of bar buckling, but bar buckling is not required for boxy/peanut-shape formation. Friedli & Pfenniger (1990) reported that N-body simulations that forced z-symmetry did grow boxy/peanut-shaped bulges but more slowly than those that did not force the symmetry.

In Figure 6 and 7 we show snapshots of the gS0 simulation. Figure 6 shows the gS0 simulation just after bar growth and during the bar buckling phase. Figure 7 shows the gS0 simulation at later times. During the bar buckling phase, the peanut shape is quite strong but smaller than at later times. The peanut shape resembles a W-shape with two upper widely separated peaks at large radius above the plane and two less widely separated peaks below the plane. As was true in the gSa simulation, the peanut shape in the gS0 simulation becomes longer at later times. In both simulations discussed here, the bar pattern speed does not remain fixed, but slows down after bar growth. Pattern speeds as a function of time are shown in Figure 2 by Minchev et al. (2012).

We compute the Fourier coefficients of the stellar disk density from the simulation snapshots in a grid of radial and vertical positions;  $S_m(r, z) \equiv \frac{1}{\pi} \int \rho(r, z, \phi) \cos m\phi d\phi$ , where  $\rho(r, z, \phi)$  is the stellar density. In Figures 8 and 9 we show these Fourier coefficients, as a function of  $r, z$ , divided by the axisymmetric average of the density at each radius and height,  $S_0(r, z) \equiv \frac{1}{2\pi} \int \rho(r, z, \phi) \cos m\phi d\phi$ . The peanut-

shape is particularly evident at later times in these images. The peanut-shape in these normalized Fourier components is wider (in height) than the peanut shape in the actual density distribution. This implies that above the disk, the fraction of stars aligned with the bar is larger than the fraction of stars aligned with the bar in the mid plane.

During bar-buckling, the first order Hamiltonian model should model the resonance (equation 12). Inside resonance (negative  $\delta$  and at smaller radius), periodic orbits are found at  $\phi = \pi$ , whereas outside resonance (positive  $\delta$ ), periodic orbits have  $\phi = 0$  (see Figure 4). Outside resonance banana shaped periodic orbits oriented with the buckling support the buckling, having high  $z$  at the ends of the bar, whereas inside resonance, periodic orbits have low  $z$  at the ends of the bar. The W-shape in Figure 6 may be consistent with this Hamiltonian model. The two inner radius apexes of the W may correspond to the banana shaped orbits inside resonance with the banana ends pointing down, whereas the two outer upper ends of the W could be from banana-shaped orbits with the two ends oriented upward. The width of the resonance is set by the libration frequency ( $\tau_{lib}^{-1}$ ) and depends on the resonance strength (equation 14). As the resonance weakens, the libration frequency decreases and the resonance is strong over a smaller range of radius. Consequently, when the asymmetric perturbation is strong at early times, the two peaks in the W are far apart, but they approach each other as the buckle weakens at later times. The progression is as seen in Figure 6. This progression of the classes of orbits has also been illustrated by Martinez-Valpuesta et al. (2006) by searching for periodic orbits in N-body snapshots. When the galaxy becomes more symmetrical the first order resonant term weakens and the second order one dominates. The resonant model becomes second order (equation 3), and both sides of resonance contain both classes of banana shaped orbits, as shown in Figure 1. The transition is illustrated in a varying Hamiltonian model in Figure 4 from top to bottom showing the growth of the downward facing banana shaped periodic orbits appearing as the buckling dies away.

Depending upon the speed of evolution of the perturbations, the distribution of upwards oriented banana-shaped orbits may differ from the distribution of downward oriented banana-shaped orbits after the buckling has dissipated.

#### 3.1 Estimating oscillation frequencies in the simulations

We describe how we measure the angular rotation rate,  $\Omega$ , vertical oscillation frequency  $\nu$ , and epicyclic frequency,  $\kappa$ , as a function of radius in individual simulation snapshots.

Because the halo is live, the center of the galaxy does not remain fixed. To measure quantities as a function distance from the galaxy center, the bulge center at each timestep must be taken into account. At every timestep we computed centroids in the central region using stars with coordinate radius inside  $r < 2$  kpc. Velocity and position centroids computed from all stars in this central region were subtracted before making additional measurements. In the annulus  $4 < r < 5$  kpc we computed the  $m = 2$  Fourier components of the mass distribution projected onto the mid-plane. This gives a measurement of the bar orientation angle. The stars were then rotated so that the bar was oriented horizontally for all subsequent computations. Bar pattern

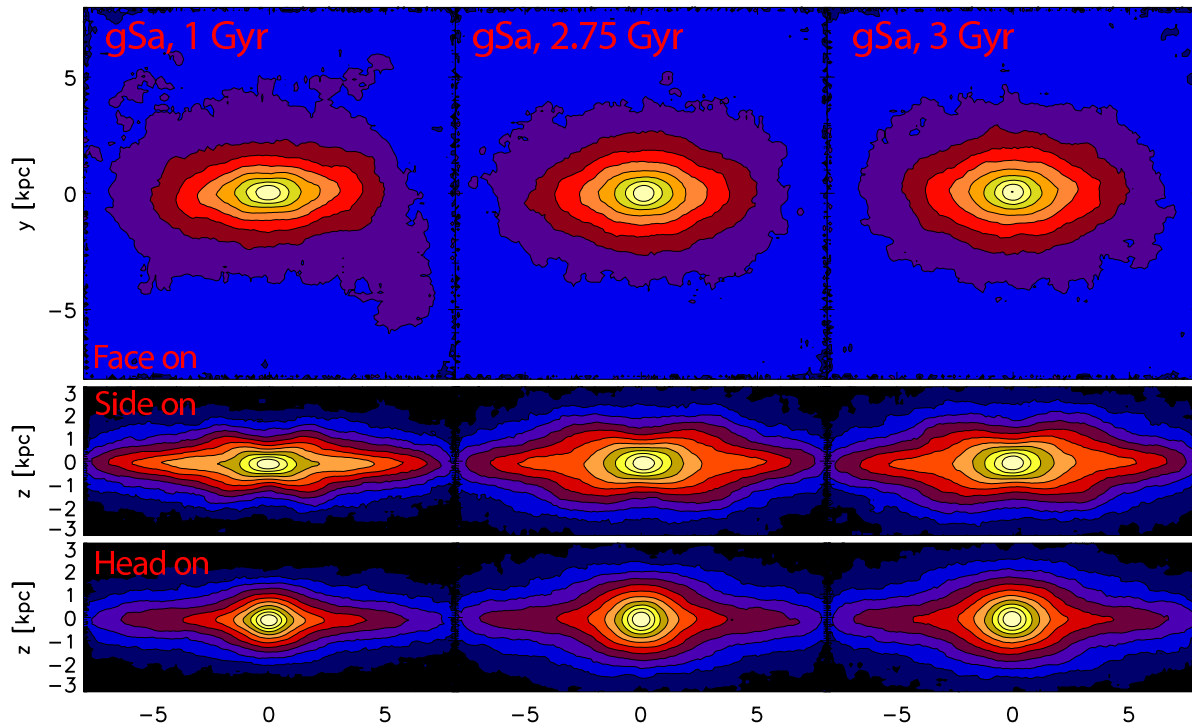


**Figure 5.** Simulation snapshots are shown for three different times (1.0, 2.75, 3.0 Gyr) during the gSa GalMer simulation. Top panel shows projected disk density on the  $xy$  plane with  $x$  aligned with the bar. The middle and bottom panels show projected density on the  $xz$  and  $yz$  planes. Axes are in kpc. Only disk stars are shown. The bar is not at a fixed pattern speed, but continues to slow down. The peanut shape continues to grow.

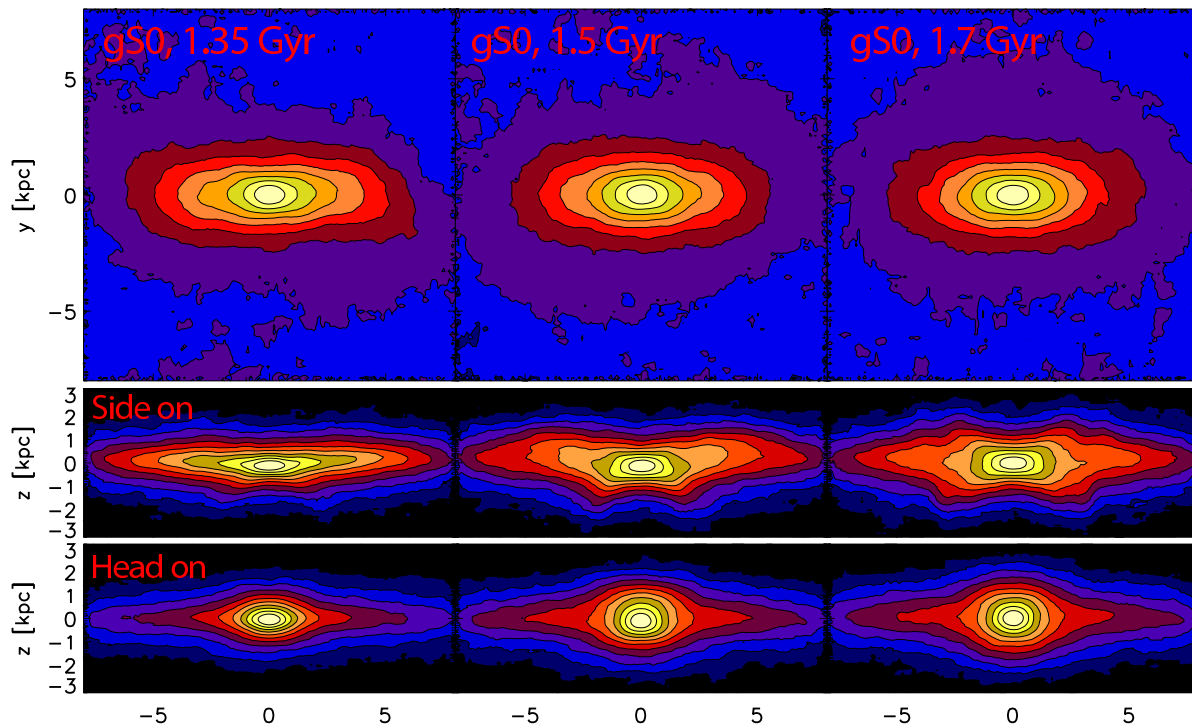


**Figure 6.** Simulation snapshots are shown for the gS0 simulation during bar buckling and at 1.35, 1.5 and 1.7 Gyr. Similar to Figure 5. During bar buckling the bar exhibits a W shape with two outer peaks separated by a large radius above the plane and two inner because less separated below the plane. The peaks of the W are closer together at later times than at earlier times.

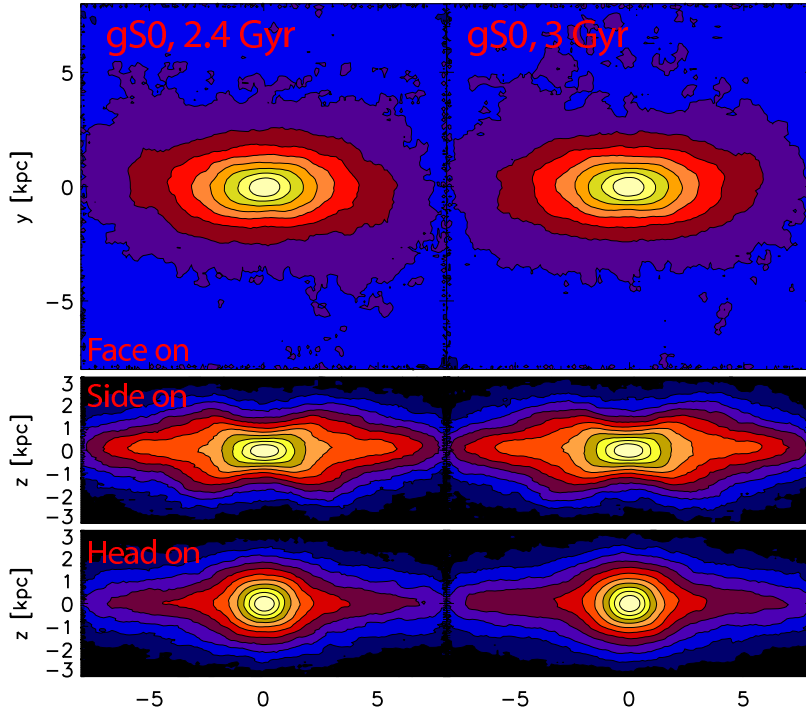


**Figure 7.** Simulation snapshots are shown for the gS0 simulation at 2.4 and 3.0 Gyr long after bar buckling. Similar to Figure 5. The peanut length is longer than during bar buckling. The bar is not at a fixed pattern speed, but continues to slow down.

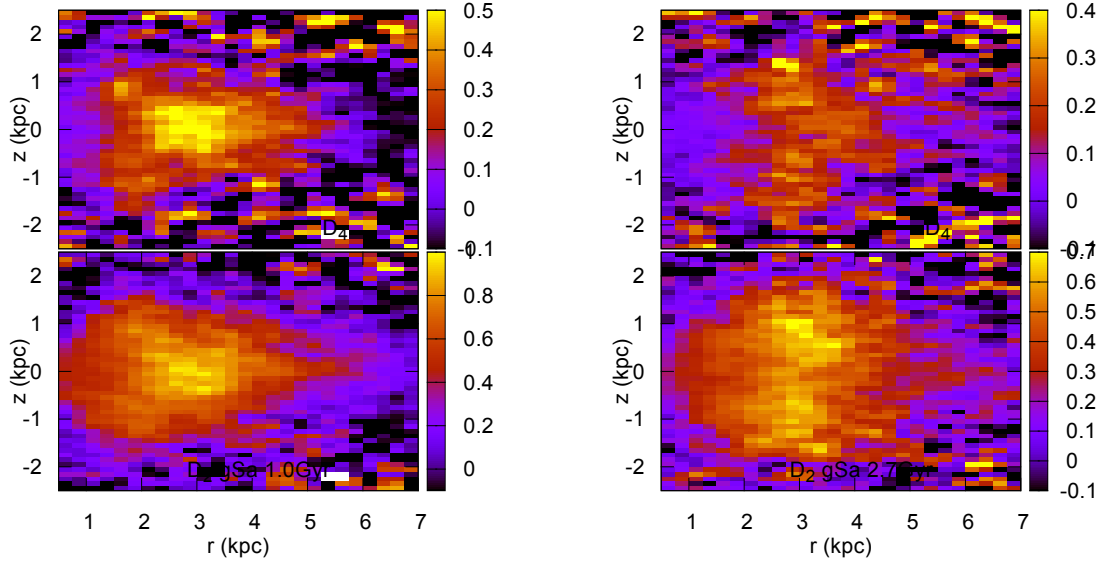


**Figure 8.** Fourier components of the disk density as a function of radius and height. The  $m = 2$  and  $m = 4$  Fourier coefficients of the density distribution are shown, divided by the axisymmetric value, for the gSa simulation at 1.0 (left) and 2.7 Gyr (right). The top of each panel shows the  $m = 4$  Fourier coefficient and the bottom of each panel the  $m = 2$  coefficient as a function of radius and of height. The value at each position is shown divided by the axisymmetric value at that radius and height. The  $x$  axes are radii and the  $y$  axes are height  $z$  above or below the galactic plane, both in kpc. The X-shape is visible at later times in the shape of the  $m = 2$  Fourier coefficient (see panel on lower right).

speeds were measured from the advance of the bar angle as a function of time and were consistent with those plotted in Figure 2 by Minchev et al. (2012).

Many GalMer simulations are archived with an array giving the gravitational potential at the position of every star. We used this to estimate the azimuthally averaged po-

tential in the mid plane as a function of radius and height. To reduce the graininess caused by the halo particles, we also computed the Fourier components by direct summation as a function of height using the positions and masses of the stars alone.

Vertical slices of the azimuthally averaged gravitational

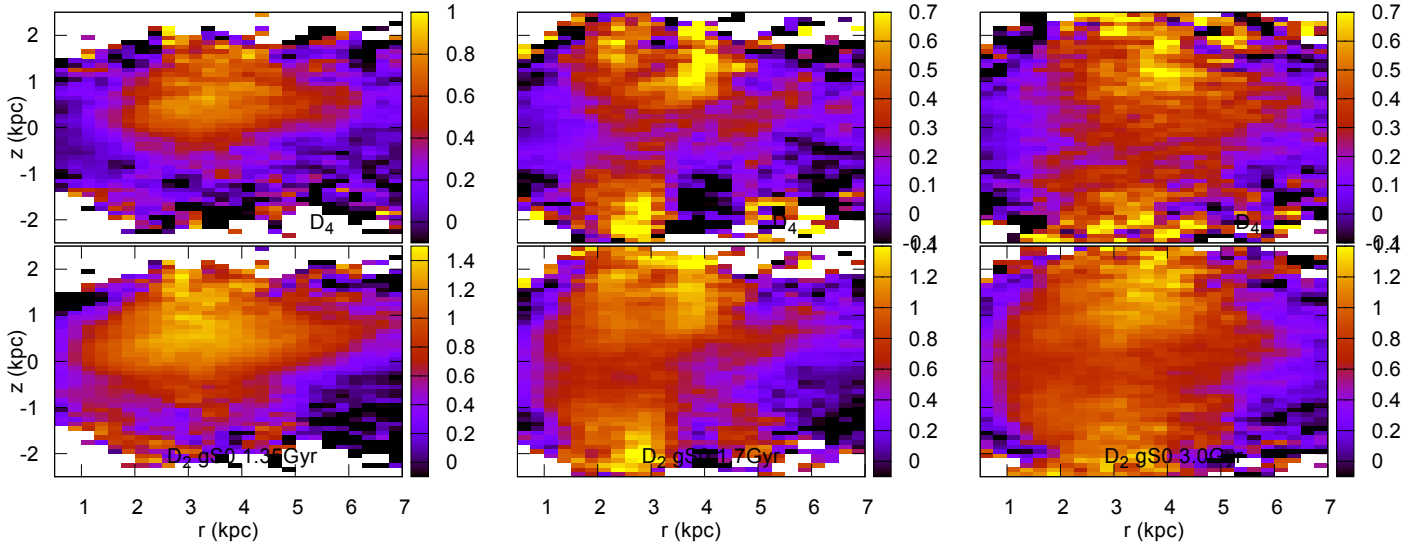


**Figure 9.** Normalized Fourier  $m = 2$  and  $m = 4$  components of the density as a function of radius and height. Similar to Figure 8 except for the gS0 simulation and at 1.35, 1.7 and 3.0 Gyr.

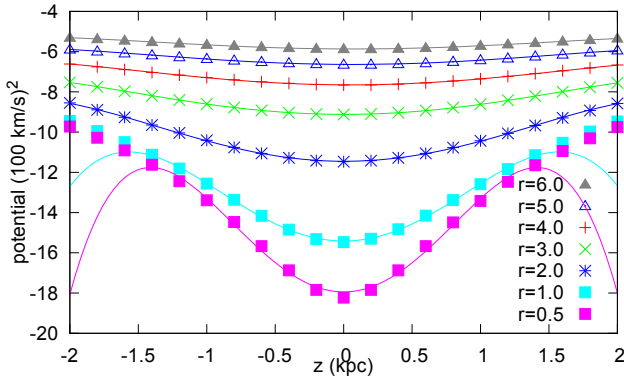


**Figure 10.** Shape of the azimuthally averaged gravitational potential as a function of  $z$  at different galactocentric radii in the mid-plane. Fits to the potential are shown as lines. These fits are used to estimate the vertical oscillation frequency,  $\nu$ , and the parameter  $\lambda$ . This figure shows fits for the gS0 simulation at 1.7 Gyr.

potential at different radii are shown in Figure 10 for a single snapshot. The profiles are centered on zero implying that the centroiding was effective. At each radius, we fit a quadratic function as a function of  $z$ . Both the profiles (measured from a simulation snapshot) and the fits are shown in Figure 10 at two different times. These functional fits are used to compute the vertical oscillation frequency,  $\nu$ , and parameter

$$\lambda = \left. \frac{\partial^4 V_0}{\partial z^4} \right|_{z=0} \quad (25)$$

at different radii. The parameter  $\lambda$  is needed for computation of the  $a$  coefficient in the Hamiltonian (see appendices A and B). We checked that the measurements for  $\lambda$  and  $\nu$  were not strongly dependent upon the form of the function fit to the potential or the method used to compute the azimuthal average.

A polynomial function,  $f(r) = a_0 + a_1 r + a_2 r^2 + a_3 r^3 +$

$b_0 \log(r) + b_1/r + b_2/r^2$ , was fit to the azimuthally averaged potential,  $V_0(r)$  in the mid-plane. Inverse and logarithm terms were used so as to allow the potential to diverge at the origin. The coefficients  $a_0, a_1, a_2, a_3$  have units of  $(\text{km/s})^2$ ,  $(\text{km/s})^2 \text{ kpc}^{-1}$ ,  $(\text{km/s})^2 \text{ kpc}^{-2}$  and  $(\text{km/s})^2 \text{ kpc}^{-3}$  respectively. The coefficients  $b_0, b_1, b_2$  have units  $(\text{km/s})^2$ ,  $(\text{km/s})^2 \text{ kpc}^1$ , and  $(\text{km/s})^2 \text{ kpc}^2$ . This function was then differentiated to estimate the angular rotation rate and epicyclic frequency

$$\Omega(r) \equiv \sqrt{\frac{1}{r} \frac{\partial V_0}{\partial r}} \quad \kappa(r) = \sqrt{3\Omega^2 + \frac{\partial^2 V_0}{\partial r^2}}, \quad (26)$$

both evaluated at  $z = 0$ . These frequencies are shown along with the bar pattern speed at early and late times in the simulations in Figure 11. The bar pattern speed is shown as a horizontal line in this figure. The location where the bar pattern speed crosses  $\Omega$  is approximately consistent with a corotation radius estimated from 1.2 times the bar length. The approximate location of the vertical resonance can be estimated from where the bar pattern speed line,  $\Omega_b$ , crosses  $\Omega - \nu/2$ . Because the bars slow down and the disk thickens, the vertical resonance is at a larger radius at later times in both simulations.

Combes et al. (1990) found that  $\nu \sim \kappa$  near the 2:1 vertical resonance and so the 2:1 vertical and Lindblad resonances were essentially on top of one another. However, Figure 11 shows that the vertical resonance lies outside the Lindblad resonance (where  $\Omega_b$  intersects  $\Omega - \kappa/2$ ). Orbits are primarily aligned with the bar outside the Lindblad resonance and perpendicular to the bar inside the Lindblad resonance. Consequently, orbits in the vicinity of the vertical resonance should be aligned with the bar. Periodic orbits (in three dimensions) would be banana shaped. They would be elongated along the bar and reach high inclinations at the ends of the bar. If the vertical resonance were inside the Lindblad resonance then the periodic orbits could be at high inclinations at the ends of the bar but the orbits would be aligned perpendicular to the bar.

It is convenient that the Lindblad resonance (where  $\kappa \sim 2(\Omega - \Omega_b)$ ) is not in the same place as the vertical 2:1 Lindblad resonance (where  $\nu \sim 2(\Omega - \Omega_b)$ ). Near the vertical resonance, the frequency  $\Delta = \kappa - 2(\Omega - \Omega_b)$ , setting distance to the 2:1 Lindblad resonance, is not slow and so bar potential perturbations with form  $\cos(\theta_r - 2(\theta - \Omega_b t))$  can be taken into account with an approximation to first order in epicyclic amplitude (see appendix D where the eccentricity of a periodic orbit is estimated). BAN+ and BAN- periodic orbits are those that have both fixed  $J_r$  and  $J_z$ . The angular momentum sets the distance  $\delta$  to the vertical resonance. For different values of  $L$ , we expect that the Jacobi integral of BAN+ and BAN- orbits is more strongly dependent on the  $J_z$  value of the periodic orbit (see equations 19, 20) in the vicinity of the vertical resonance than on the  $J_r$  of the periodic orbit.

Pfenniger & Friedli (1991) discussed orbits that have a single vertical oscillation per rotation period in the bar frame. Periodic orbits in this family were called ‘anomalous’ (Heisler et al. 1982). This resonance is associated with the resonant angle  $\theta_z - (\theta - \Omega_b t)$  and so occurs where  $\nu \sim \Omega - \Omega_b$ . We find that  $\nu > \Omega$  even at small radius in these simulations and so we did not find a region where  $\nu \sim \Omega - \Omega_b$  corresponding to a 1:1 vertical resonance associated with ‘anomalous orbits’. These orbits could exist in simulations of other galaxies.

Because the vertical resonance is not on top of the Lindblad resonances, orbital eccentricity within the bar can be estimated to first order in the epicyclic amplitude (see appendix D). We have estimated the resonance location using a mean radius, but the orbits should have a distribution with eccentricity approximately equal to that of the oval periodic orbits in the mid plane. If the orbital eccentricity is  $e$  then the distance along the bar axis is approximately  $(1 + e)r_c$  where  $r_c$  is the average radius. As the bars in both are simulations are relatively weak, we ignore the eccentricity of the orbit when comparing the location of the peanut (as seen along the bar major axis) to the location of the resonance (estimated from the mean radius).

For both simulations the location of the vertical resonance (where  $\delta \sim 0$ ) is approximately consistent with the location of the peanut shape. In the gS0 simulation during bar buckling the disk thickness increased at a radius of about 2 kpc. However the peanut shape at later times grew to larger radii of 3-4 kpc. The location of the peanut-shape seen in the mass distribution is consistent with the location of the vertical resonance at both early and later times, confirming the results of the periodic orbit study by Combes et al. (1990); Martinez-Valpuesta et al. (2006). This suggests that the location of the vertical resonance is more important than a previous history of bar buckling in determining the final location and height of the peanut-shape. The gSa simulation supports this interpretation as the peanut length is also consistent with the location of the resonance, even though the bar did not buckle in this simulation.

### 3.2 Bar perturbations

The  $m = 2$  and  $m = 4$  Fourier coefficients as a function of  $z$  and  $r$  of the gravitational potential, divided by the mid plane circular velocity  $v_c^2(r)$ , are shown in Figure 12 and 13. Because we work in a frame aligned with the bar, only cosine

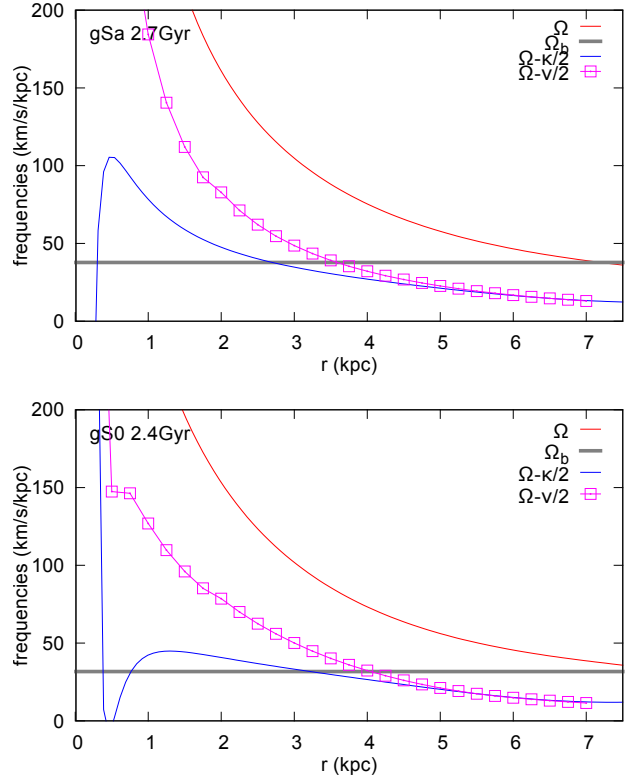
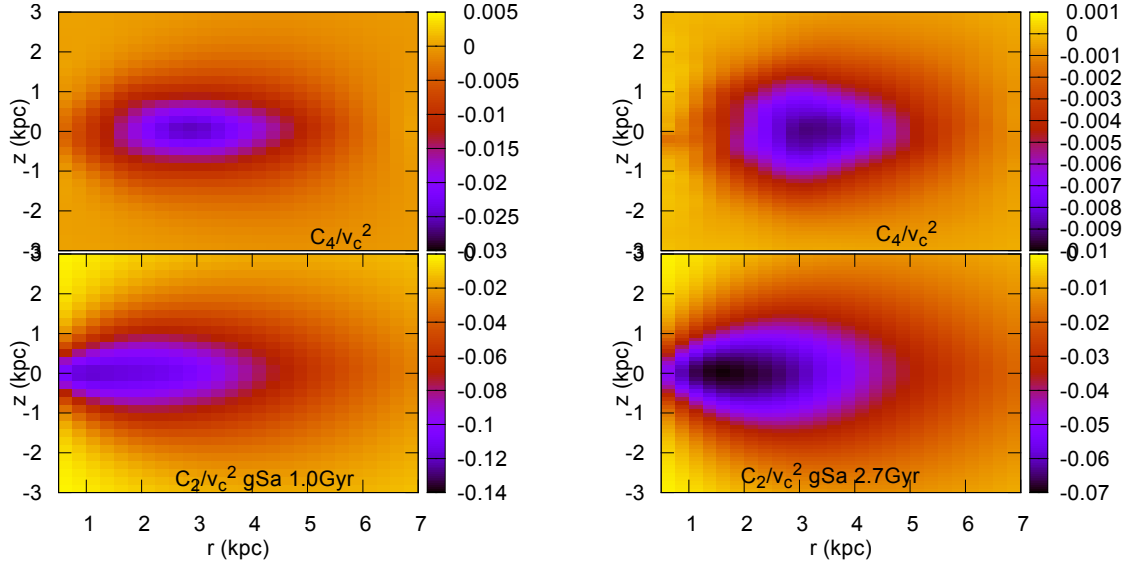


**Figure 11.** Location of vertical and Lindblad resonances as estimated from the potential fitting. A polynomial function that included inverse and logarithmic terms was fit to the mid-plane potential. This function was then differentiated to estimate the angular rotation rate and epicyclic frequency,  $\Omega$  and  $\kappa$ . Derivatives of the functions fit to the vertical shape of the axisymmetric potential (with an example shown in Figure 10) are used to estimate the vertical oscillation frequency,  $\nu$ . The approximate location of the vertical resonance can be estimated from where the bar pattern speed line,  $\Omega_b$  (shown as a horizontal line), crosses  $\Omega - \nu/2$  (plotted as points). If the bar slows down, or the disk thickens, the vertical resonance can be at a larger radius at later times. The vertical resonance (associated with banana orbits) lies outside the Lindblad resonance (where  $\Omega_b$  intersects  $\Omega - \kappa/2$ ; plotted with a blue line). Consequently, orbits in the vicinity of the vertical resonance should be aligned with the bar. a) For the buckling-lacking gSa simulation at  $t = 2.7$  Gyr. b) For the bar-buckling gS0 simulation at  $t = 2.4$  Gyr. For both simulations the length of the peanut-shape is approximately consistent with the radius of the vertical resonance.

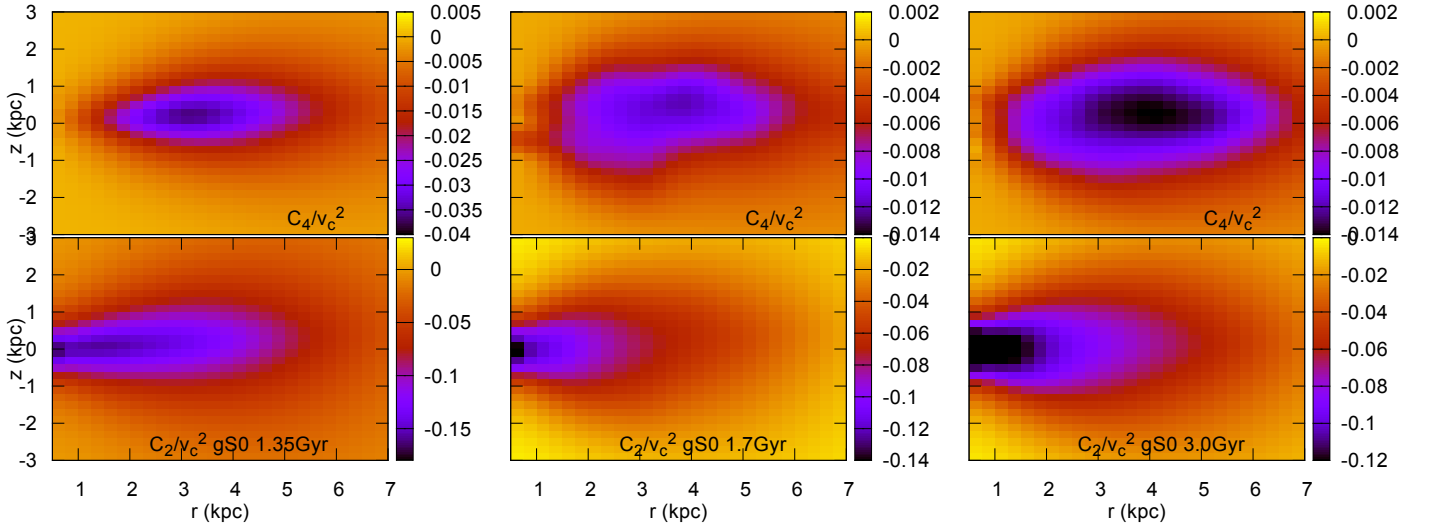
components are nonzero. The bar also gives strong vertical perturbations in the  $m = 4$  Fourier component as seen from the top panels in these figures. This is relevant because when the galaxy is symmetrical about the midplane, the vertical resonance strength is dependent upon the vertical structure of the  $m = 4$  coefficient.

Figure 15 shows examples of the Fourier components as measured from a single snapshot at different radii and as a function of  $z$ . We fit a quadratic function to each of these sets of points, approximating the bar perturbation as

$$V_b(\theta, r, t) = \left[ C_2(r) + B_{2z}(r)z + C_{2z}(r)z^2 \right] \cos(2(\theta - \Omega_b t)) + \left[ C_4(r) + B_{4z}(r)z + C_{4z}(r)z^2 \right] \cos(4(\theta - \Omega_b t)) \quad (27)$$



**Figure 12.** The bar perturbation  $m = 2$  and  $m = 4$  Fourier coefficients of the gravitational potential normalized by the square of the circular velocity. The coefficients are shown as a function of radius and  $z$  and computed from the gSa simulation at time 1.0 and 2.7 Gyr, left and right, respectively. The top of each panel shows the  $m = 2$  Fourier coefficient and the bottom of each panel the  $m = 4$  coefficient. The  $x$  axes are radii and the  $y$  axes are  $z$ , both in kpc. The potential Fourier components are shown in units of  $(100 \text{ km/s})^2$ .



**Figure 13.** The bar perturbation  $m = 2$  and  $m = 4$  Fourier coefficients of the gravitational potential normalized by the square of the circular velocity. Similar to Figure 12 except for the gS0 simulation and at 1.35, 1.7 and 3.0 Gyr.

with the result of our fitting giving us values for  $C_2, B_{2z}, C_{2z}, C_4, B_{4z}, C_{4z}$  as a function of radius. The measurements for the coefficients  $C_{2z}, C_{4z}$  as a function of radius for different snapshots in the two simulations is shown in Figure 16 and illustrate that the quadratic function is an adequate fit.

The coefficient  $C_{4z}$  determines the  $\epsilon_s$  coefficient for our second order Hamiltonian model. In the vicinity of the vertical resonance with resonant angle  $\theta_z - (\theta - \Omega_b t)$  (where there is a single vertical oscillation per orbit in the bar's frame) the coefficient  $\epsilon_s$  would depend on  $C_{2z}$ . During bar buckling  $B_{2z}$  contributes to  $\epsilon_b$  for the first order Hamiltonian model. The  $C_{2z}, C_{4z}$  coefficients are positive as expected. As long

as the coefficient  $a$  remains negative, periodic orbits would be banana shaped and so support a peanut shape.

Previous work has used as a measure of bar strength the parameter  $Q_T$  (Combes & Sanders 1981). At a given radius this is the ratio of the maximum tangential force to the azimuthally averaged radial force in the mid-plane. Using the  $m = 2$  component and equation 27, we find  $Q_T \approx \frac{2C_2(r)}{v_c^2}$ . We use figures 12 and 13 (giving  $C_2$  at  $z = 0$ ) to estimate  $Q_T \sim 0.2$  for both simulations. These would be classified as weak bars in comparison to the sample studied by Laurikainen et al. (2004).

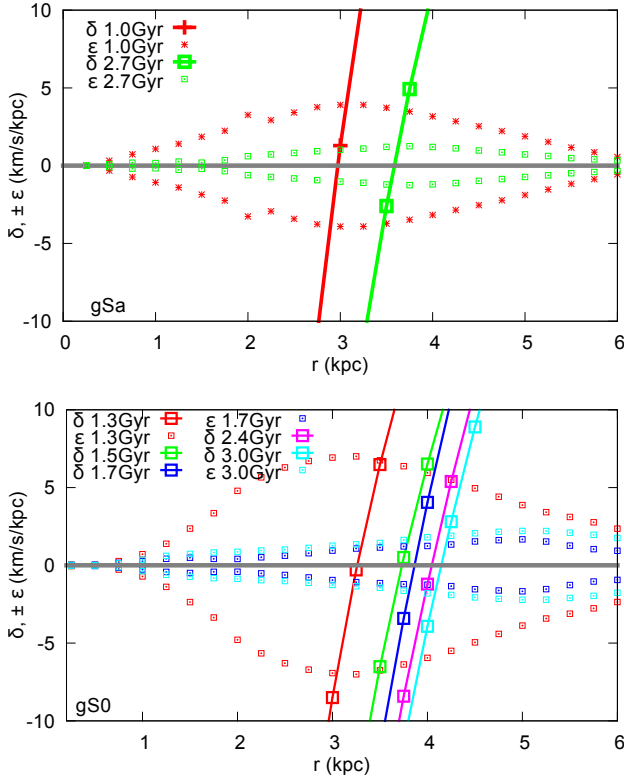


**Figure 14.** How the vertical resonance location varies at different times. Here distance to resonance  $\delta = \nu - 2(\Omega - \Omega_b)$  is plotted as a function of radius but at different times in the simulation. Also plotted are perturbation strength  $\epsilon_s$  values (approximately the resonant libration frequency) estimated from the  $m = 4$  Fourier components of the potential. Values for  $\delta$  and  $\pm\epsilon_s$  for each snapshot are given the same color. The width of the resonance and extent of the peanut-shape or bow-tie shape can be estimated by taking the radius where  $\delta$  for each color crosses the lower set of similar color points (where  $\delta = -\epsilon_s$ ) to where  $\delta$  crosses the higher set of similar color points (where  $\delta = \epsilon_s$ ). a) In the buckling-lacking gSa simulation. b) In the bar-buckling gS0 simulation. At times  $t = 1.35 - 1.7$  the bar buckles and the disk thickens. This decreases the vertical oscillation frequency,  $\nu$ , moving the resonance outward. In both simulations the bar slows down at later times, moving the resonance outward.

### 3.3 The vertical resonance location and its width

Using the coefficients for the potential perturbation strength we can estimate the libration frequency (equivalent to  $\epsilon_s$ ; see equation 15) in resonance. Using equation 9 we compute the resonance libration frequency from the  $m = 4$  bar perturbation strength  $C_{4z}$  (shown in Figure 16) and the vertical oscillation frequency,  $\nu$ . Libration frequencies are also plotted in Figure 14. Recall from the discussion above (section 2.1) that the resonance width can be estimated from the condition  $|\delta| \lesssim |\epsilon_s|$ . In Figure 14 we have plotted  $\delta$  with estimates for  $\pm\epsilon_s$  so these two quantities can be directly compared. We find that the resonance libration frequency, estimated from the bar perturbation strength, is approximately 1-2 km/s/kpc. The range of radius that satisfies  $|\delta/\epsilon_s| < 1$  is small,  $\approx 0.1 - 0.3$  kpc. This range in radius corresponds to  $dr/r \sim 0.05$  about resonance commensurability or in an-

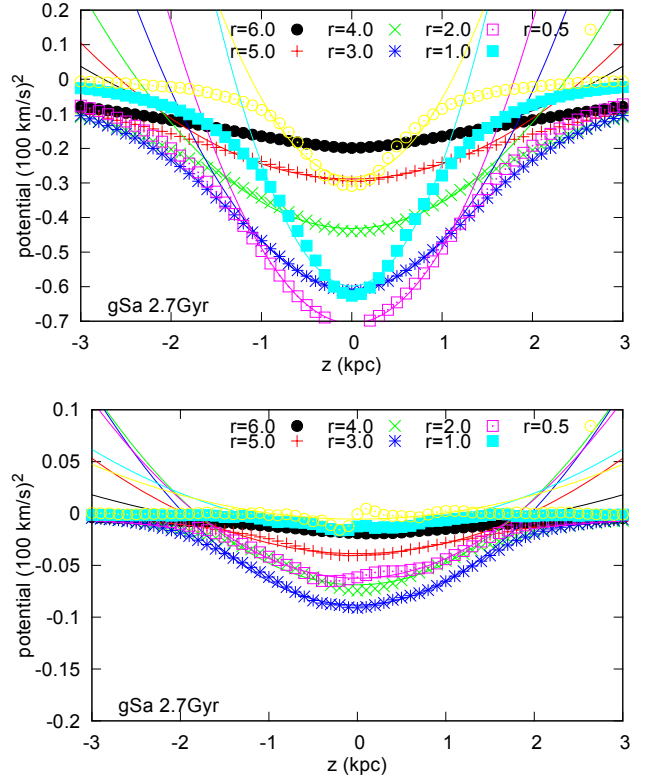


**Figure 15.** Fits to the vertical structure of Fourier components of the bar potential. A quadratic function was fit to the potential profile extracted at different radii. The potential profile at each radius is shown with a different color point and the accompanying fit with the same colored line. Shown here are the points and fits to the gSa simulation at  $t = 2.7$  Gyr. a) For  $m = 2$  giving parameters  $C_2$  and  $C_{2z}(r)$ . b) For  $m = 4$  giving parameters  $C_4$  and  $C_{4z}(r)$ .

gular momentum  $r dL/L \sim 0.05$ . The resonance can only affect orbits in a small region of phase space.

The resonant width is significantly narrower than the extent of the peanut seen in the Fourier components (for the density Figures 8 and 9, for the potential Figures 12 and 13). Quillen (2002) suggested that an X-shape or bow-tie shape was formed due to the linear dependence of the fixed point height on  $\delta$  between  $-\epsilon_s < \delta < \epsilon_s$ . Here we find that this radial region is far too small to account for the extent of the observed peanuts or X-shape in the Galactic bulge. Hence the resonance capture model fails to predict the X-shape.

The association of the resonance with the feature is robust. The Hamiltonian model implies that banana shaped orbits are not found distant from resonance. We see that the resonance moves outwards during the simulation, consequently we must consider the situation illustrated in Figure 2. In this setting stars originally in the mid plane outside of resonance are lifted to high inclination as they encounter the resonance. They must go into orbits just inside the separatrix until the separatrix shrinks leaving them in high inclination orbits but with circulating  $\phi$  and so no longer supporting the peanut-shape. While the stars are inside the resonance, their height would be similar to the separatrix height (equation 21). In this heating model, the only stars

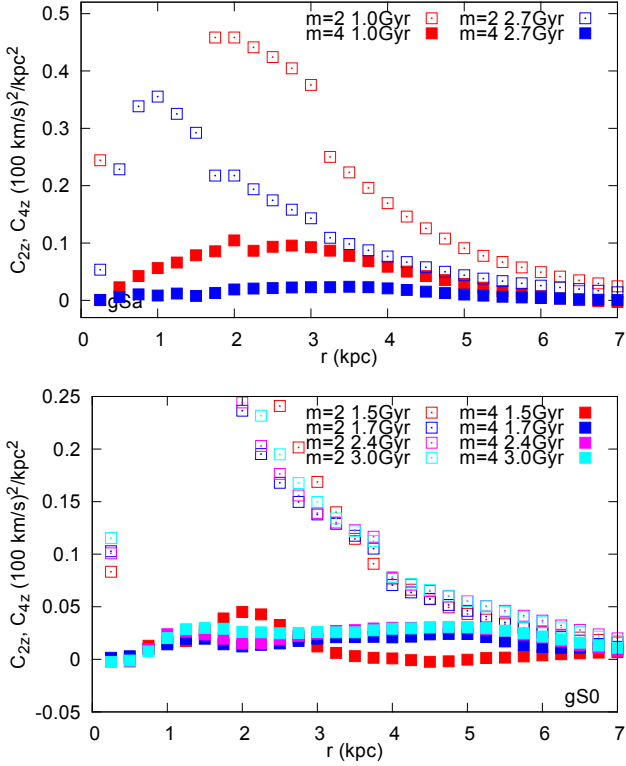


**Figure 16.** Quadratic coefficients  $C_{2z}, C_{4z}$  for the vertical bar perturbations at different radii and at different times. a) For the gSa simulation. b) For the gS0 simulation. These coefficients arise from the fits to the Fourier components of the gravitational potential as a function of  $z$ . The vertical perturbations from the bar are stronger at earlier times in the gSa simulation.

that support the peanut shape are those that have just entered the resonance or those that have just left and remain near the separatrix. In this scenario, the peanut shape is due to a small number of stars in or near resonance. This implies that they must have very similar angular momentum values. This follows as orbits that support the peanut only exist in the vicinity of resonance. The X- or peanut shapes seen in galaxies must trace the narrow volume of the possible orbits that can support the peanut.

Because the  $C_{2z}$  and  $C_{4z}$  coefficients depend on the second derivative of the gravitational potential with respect to  $z$ ,  $\partial^2 V_b / dz^2$ , we expect that

$$\begin{aligned} |C_{2z}| &\sim \left| \frac{C_2 \nu^2}{v_c^2} \right| \\ |C_{4z}| &\sim \left| \frac{C_4 \nu^2}{v_c^2} \right|, \end{aligned} \quad (28)$$

where  $C_2/v_c^2$  and  $C_4/v_c^2$  are the amplitudes of the  $m = 2$  and  $m = 4$  Fourier coefficients of the potential in the mid plane due to the bar perturbation. These can be estimated using the images shown in Figures 12 and 13. This implies that the resonant width or frequency  $\epsilon_s \sim \nu \frac{C_4}{v_c^2}$  or  $\frac{\epsilon_s}{\nu} \sim \frac{C_4}{v_c^2}$ . The mid plane  $m = 4$  Fourier component of the potential are at most 0.01 (in units of  $v_c^2$ ) and so we estimate that  $\frac{\epsilon_s}{\nu} \sim 0.01$ . This is approximately consistent with the 1-2 km/s/kpc frequency we measured for  $\epsilon_s$  directly.

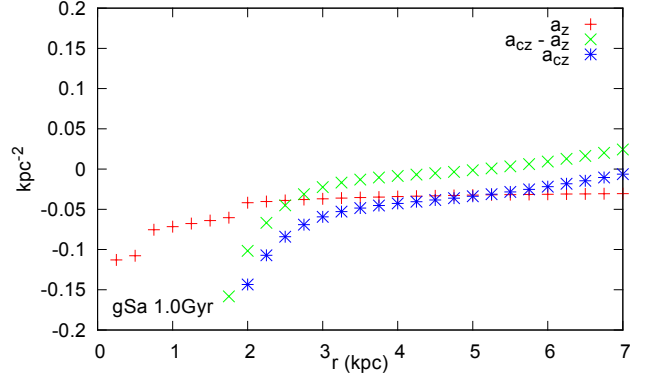


**Figure 17.** Functions  $a_z$  and  $a_{cz}$ , (computed using equations A13 and B6) and their difference are plotted here using fits to the potential of the gSa simulation at 1Gyr. The coefficient  $a_{cz}$  is needed to compute the heights of stars in resonance.

For a fixed bar shape, setting  $C_4$ , the quantity  $C_4/v_c^2$  should not significantly vary. However if the disk thickens then  $\nu$  decreases. This would have the effect of reducing  $\epsilon_s$  and so the strength of the resonance. The frequency  $\epsilon_s$  is weaker at later times than earlier ones for the gSa simulation (as seen from the distance between red points and between green points showing  $\pm \epsilon_s$  in Figure 14a). The reduction may be in part due to disk thickening rather than the bar becoming rounder.

### 3.4 Vertical excitation in resonance

We now discuss the vertical excitation caused by the resonance. In the resonant heating models  $z_{sep}$  sets the height of the peanut. Recall that  $z_{max}$  is the height of the fixed points (or periodic orbits) where  $\delta = \epsilon_s$ , at the outer edge of the resonance and  $z_{sep}$  is the maximum height of an orbit in the separatrix at the same  $\delta$  (equation 21). Equation 21 depends on the  $a$  coefficient that depends on fourth order derivatives of the potential. The coefficient  $a$  is derived in appendix B (where  $a = a_{cz}$ ; equation B6) using a fourth order approximation in epicyclic and vertical oscillation amplitudes. The coefficient given in equation B6 contains three terms. The second two both have larger magnitude than the first that we denote  $a_z$  that only depends on  $z$  derivatives of the potential. When we compute them from our fits to the gravitational potential, we find that the two larger terms approximately cancel leaving a coefficient with  $a_{cz} \sim a_z \sim -0.05 \text{ kpc}^{-2}$  in the vicinity of the peanut in all simulations. An example of the  $a_z$  and  $a_{cz}$  coefficients computed for one of the simulation snapshots (computed using equations A13 and B6) is shown in Figure 17. We took into account the corrections derived in appendices A and B (see equation B6) and were surprised to find that  $a_z$  was a reasonable approximation to  $a_{cz}$ .

Figure 18 shows as small points the separatrix height,  $z_{sep}$ , as a function of radius calculated using equation 21 and  $a = -0.05 \text{ kpc}^{-2}$  and using our measurements for  $C_{4z}$  and oscillation frequencies. The height is computed for both simulations and for different snapshots. As solid curves, the locations of the resonance are shown as narrow Gaussians. In the resonance heating model stars are lifted to  $z \sim z_{sep}$

as they enter the resonance. They then leave the resonance, remaining at high inclination but are no longer oriented with and supporting the peanut shape. As the resonance passes through the disk, the disk is heated and should remain at approximately a height of  $z_{sep}$ . Stars supporting the peanut shape and in resonance should have a height approximately of  $z_{sep}$ . From Figure 18 we see that the predicted peanut height is approximately 1 kpc, is consistent with the height of the observed peanut shapes. Even though the resonance is thin and weak, because  $a$  is small, the resonance height is not insignificant. The coefficient  $a$  acts somewhat like a mass in a harmonic oscillator system. A weak spring can cause a higher amplitude oscillation on a low mass than a high mass.

### 3.5 Interpretation of the X-shape

Because the resonance is thin and has moved outward, the resonance capture model does not account for the X-shape of peanut shaped bulges. Here we ask again, why is an X-shape observed? As we have discussed above, stars only are aligned with and support the peanut shape if they are in resonance (and have librating  $\phi$  angle near  $0$  or  $\pi$ ) or are near resonance and are spending more time near  $0, \pi$  than near  $\pm\pi/2$  (see Figure 3). The only population of stars likely to be in resonance (have librating  $\phi$  angle) are those that have been recently captured into resonance or those that are in the vicinity of the resonance separatrix. These are disk stars that were originally in the mid plane just exterior to resonance. The X-shape then must be due to the orbital distribution of these stars or the morphology of their orbits. Here we have associated them with the vicinity of the resonance separatrix at  $\delta = \epsilon_s$  and have predicted their maximum height using the maximum height of this orbit. As can be seen from the Hamiltonian level curves (lower right panel of Figure 1), orbits within the separatrix are not periodic, instead they librate about a periodic orbit. They would support the X-shape but would fill in the region between the top of the X and the mid plane as  $\phi$  varies between  $\phi = \pm\pi/4$ .

Stars just exterior to the resonance separatrix (see Figure 3) spend more time with  $\phi$  near  $0, \pi$  than near  $\pm\pi/2$  and so would also support the X- or peanut shape, even though the resonant angle is circulating. Stars that have left the resonance (after being lifted by it) and are distant from the resonance, are likely to be at high inclination but no longer supporting the peanut shape. Thus they would appear to be part of the bulge even though they originated as disk stars.

Previous studies have found that banana shaped orbits exist over a range of Jacobi constant,  $E_J$ , (Pfenniger & Friedli 1991; Martinez-Valpuesta et al. 2006). The Jacobi constant is the energy in the rotating frame; see the end of appendix A. Because the resonance is narrow we find that it is only important in a very small range of angular momentum. However the Jacobi energy also depends on the epicyclic action variable  $J_r$ . A periodic orbit in three dimensional space, such as in the BAN+ and BAN- families, is periodic in both radius and vertical height. They only exist in the vicinity of the vertical resonance and this essentially sets the angular momentum value because the resonance is thin. The requirement that the orbit is also periodic in radius sets the  $J_r$  value and so the Jacobi energy. We expect

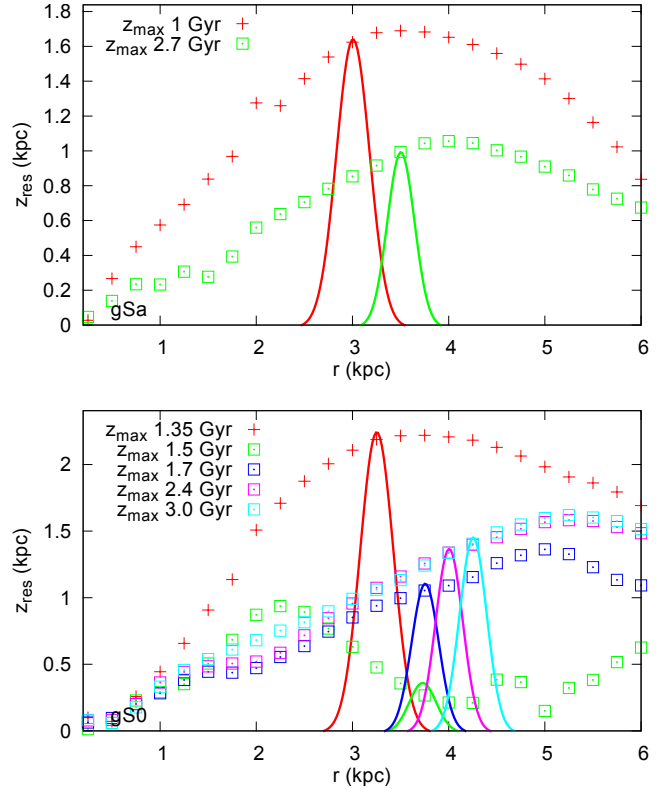


**Figure 18.** Vertical excitation height caused by the resonance. Small points show the maximum height of the separatrix,  $z_{sep}$  (equation 21), in kpc as a function of radius. The location of the resonance at different times is shown as solid Gaussians. a) For the gSa simulation and computed using potential measurements from different snapshots. b) Similarly for the gS0 simulation. In both simulations, the resonance moves outward. As stars in the mid plane outside resonance enter the resonance, they are forced out of the mid plane to a height approximately given by  $z_{sep}$ . While in resonance, they lie just inside the separatrix. As the separatrix shrinks they leave resonance but remain at high inclination.

that the banana shaped periodic orbits only exist over a narrow range of energy.

However, within the context of the resonance heating model, stars are not captured into orbits near the periodic orbit families but rather spend time near the vertical resonance separatrix. Furthermore, the vertical resonance need not affect the radial degree of freedom. Stars of different values of eccentricity (or  $J_r$ ) and so Jacobi energy could be lifted in to orbits near the vertical resonance separatrix. The resonance is most narrowly identified by its angular momentum rather than energy. We expect that the stars supporting the X-shape would have a similar  $J_r$  distribution to the stars just exterior to resonance and so a similar distribution in Jacobi energy as exterior to resonance.

### 3.6 Velocity distributions measured along the bar

The heating scenario discussed above makes some predictions for the velocity distributions. Because the process is predominately one of heating, we do not expect to see a cold population of stars near periodic orbits. We expect that

low inclination orbits should be depleted within resonance, due to the previous passage of the resonance. Outside of resonance, the disk is undisturbed and stars can be in low inclination orbits.

We compare the velocity distributions at different locations along the bar major axis. At different local neighborhoods centered in the mid-plane and on the bar major axis, we extracted distributions of disk stars in radial velocity and vertical velocity ( $w$  or  $v_z$ ) and in angular momentum,  $L$ , and vertical velocity,  $w$ . In cylindrical coordinates each neighborhood has a radius (in the mid-plane) of  $0.2r_G$  where  $r_G$  is the galactocentric radius of the neighborhood. Within this cylinder, we extract velocity distributions for  $|z| < 0.5$  kpc and for  $|z| > 0.5$  kpc. All stars within these regions were used to create the distributions. The distributions were computed for the same times considered in previous figures and they are shown in Figures 19 - 22.

While the velocity distributions peak at low  $w$  (planar orbits) at earlier times, they are wider at later times. Only at large radius is there a population of stars in planar orbits at later times. Within the vertical resonance, there are no orbits that remain in the mid-plane. This gives a donut or double bar shape in the mid-plane velocity distributions in the peanut, that is particularly noticeable at later times in Figure 20 and that is not evident in the velocity distribution above and below the plane. The lack of planar orbits within the resonance is consistent with the resonant sweeping scenario we discussed above. In the resonant trapping model, we would expect a group of stars near periodic orbits. However, the velocity distributions are quite wide, suggesting that the resonance has primarily heated the stellar distribution.

The angular momentum, ( $L$ ), vs  $w$  distributions, shown in Figures 21 and 22 show structure, particularly at the later times. The lack of stars in planar orbits is visible at later times for  $L < 1000$  km/s kpc in both simulations in the planar distributions (Figures 21, 22). At each time and radius there is a particular angular momentum value, below which the vertical mid-plane velocity distribution is wide. We can associate this angular momentum value with that of the vertical resonance. Stars heated by the resonance are then visible in the distributions seen above and below the mid-plane. As angular momentum approximately sets the orbital period, stars in the resonance have a particular angular momentum value. As the vertical resonance is swept through the disk the vertical dispersions of stars are increased. We can identify the resonance location from this angular momentum value of about 1000 km/s kpc, corresponding to approximate  $r = 3$ , kpc and consistent with the radius estimated for the resonance at later times in both simulations. Figures 21 and 22 mid-plane distributions show that as the peanut grow, stars within the resonance increase in vertical distribution and the stars with high vertical dispersions are seen at increasing larger radii.

### 3.7 Is evolution adiabatic?

Resonance capture is only possible when the bar growth and drift rate are effectively adiabatic. The resonance is only effective at heating the stellar distribution if stars remain in its vicinity longer than a resonance libration timescale. Thus

the adiabatic limit is also relevant to estimate the effectiveness of resonant heating. The resonant libration frequency can be used to determine whether variations are adiabatic. The libration frequency, approximately equal to  $\epsilon_s$  and plotted as small points shown in Figure 14, is approximately 1-2 km/s/kpc =  $\text{Gyr}^{-1}$ . We can compare the square of this to the rate of bar pattern speed change. In the gSa simulation the bar pattern speed dropped from 40 to 30 km/s/kpc in 2 Gyr (from Figure 2 by Minchev et al. 2012) giving a rate  $\dot{\Omega}_b \sim -5 \text{ Gyr}^{-2}$ . This is only somewhat faster in magnitude than the square of the libration frequency,  $\epsilon_s^2 \approx 1 - 4 \text{ Gyr}^{-2}$  (recall that the square of the libration frequency approximately defines the adiabatic limit Quillen 2006). This implies that the drift rate is nearly adiabatic, particularly at later times when the bars don't slow down as fast. Because the evolution is nearly adiabatic stars that encounter the resonance have enough time in resonance to be lifted to  $z_{max}$ . If the drift were significantly faster then the stars would not feel the resonance passage.

## 4 CONSTRAINTS ON THE GALACTIC X-SHAPE BULGE

We assume that the X-shape distribution in red clump giants in the Milky Way bulge is at the location of the vertical resonance. This gives us a relation between the vertical oscillation frequency,  $\nu$ , the angular rotation rate and the bar pattern speed at the location of the resonance  $r_{LR}$ . Poisson's equation relates derivatives of the potential to the mass density. Hence, the vertical resonance gives us a constraint on the mass density in the mid-plane.

Poisson's equation  $\nabla^2\Phi = 4\pi G\rho$  relates the derivatives of the gravitational potential  $\Phi$ , to the local density,  $\rho$ . In cylindrical coordinates Poisson's equation is

$$4\pi G\rho = \frac{\partial^2\Phi}{\partial z^2} + \frac{\partial^2\Phi}{\partial r^2} + \frac{1}{r}\frac{\partial\Phi}{\partial r}. \quad (29)$$

Using expressions for  $\Omega$ ,  $\kappa$  and  $\nu$  in the mid-plane, we find

$$\rho(r, z = 0) = \frac{1}{4\pi G} [\nu^2 + \kappa^2 - 2\Omega^2]. \quad (30)$$

The vertical resonance, satisfies a resonant condition  $\nu = 2(\Omega - \Omega_b)$  at a radius  $r_{LR}$ . The density function

$$\rho_{LR}(r) = \frac{1}{4\pi G} [4(\Omega - \Omega_b)^2 + \kappa^2 - 2\Omega^2] \quad (31)$$

must be equal to the density in the mid-plane at  $r_{LR}$ . The right hand side only depends on the rotation curve in the mid-plane and the bar pattern speed. By fitting the rotation curve measurements and an estimate for the bar pattern speed we can compute this density function. The rotation curve and associated functions  $\Omega$ ,  $\kappa$  are estimated using tangent point velocities estimated from HI observations by Malhotra (1995), the rotation curve compiled by Sofue (2012) or that predicted with the Besançon model<sup>1</sup> (Robin et al. 2003). We use a bar pattern speed of  $\Omega_b = 54.2$  km/s/kpc consistent with  $\Omega_b/\Omega_0 = 1.87 \pm 0.2$  (Gardner & Flynn 2010; Minchev et al. 2007), where  $\Omega_0$  is the angular rotation rate at the Sun's galactocentric radius. We adopt a distance from

<sup>1</sup> <http://model.obs-besancon.fr/>

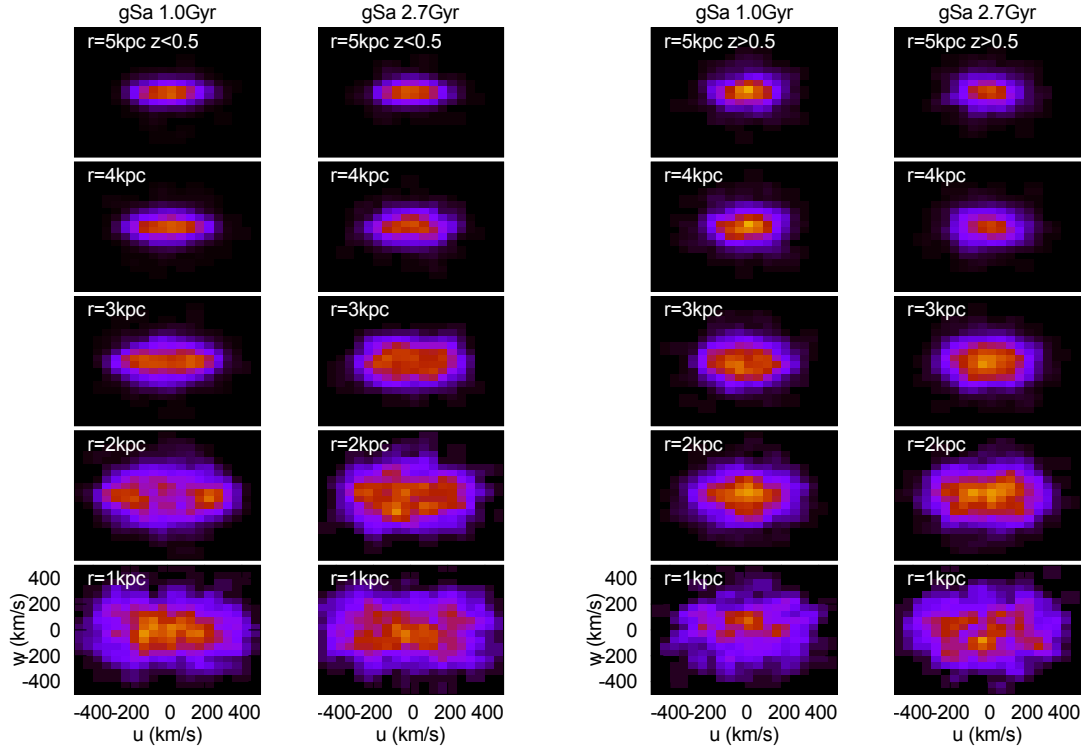


**Figure 19.** Radial ( $u$ ) vs vertical ( $w$ ) velocity distributions of disk stars generated from snapshots of the gSa simulation. Each distribution is drawn from a neighborhood centered on the bar major axis at galactocentric radius 1,2,3,4,5 kpc respectively, from bottom to top. For the left two columns, each distribution is drawn from the mid-plane (or stars with  $|z| < 0.5$  kpc) and the right two columns drawn from stars above and below the mid-plane, or stars with  $|z| > 0.5$  kpc. The first and third column (from the left) are from the snapshot at 1Gyr and the second and fourth column are from that at 2.7 Gyr.

the Sun to the galactic center of  $R_0 = 8.0$  kpc and a circular velocity of  $V_0 = 220$  km/s (Bovy et al. 2012) so that  $\Omega_0 = 27.5$  km/s/kpc.

Figure 23 shows three density functions  $\rho_{LR}(r)$  computed using equation 31 and predicted or observed rotation curves. Shown as a red line this density function is computed using the rotation curve by Malhotra (1995) based on tangent point velocities measured between  $0.2R_0$  and  $R_0$ . The green line computes the density using the Milky Way rotation curve compiled by Sofue (2012). The black line shows the density function computed from the mid plane rotation curve predicted from a Besançon model. This model has stellar and dark matter halos, thin and thick disk components, and ISM as described by Robin et al. (2003) but instead of using a point mass bulge to compute the rotation curve, we use the oblate G0 bulge model by Dwek et al. (1995) that is based on DIRBE observations, and normalized to have bulge mass  $2 \times 10^{10} M_\odot$  consistent with the Besançon model.

In Figure 23 we compare the density functions  $\rho_{LR}(r)$  to estimated mid plane densities that are shown as points on the plot. The azimuthally averaged mid plane density for the E3 bulge model by Cao et al. (2013) is shown with blue points. This has a density distribution

$$\rho_{E3}(r_s) = \rho_0 K_0(r_s) \quad (32)$$

where  $K_0$  is the modified Bessel function of the second kind and

$$r_s = \left[ \left[ \left( \frac{x}{x_0} \right)^2 + \left( \frac{y}{y_0} \right)^2 \right]^2 + \left( \frac{z}{z_0} \right)^4 \right]^{\frac{1}{4}} \quad (33)$$

The model  $E_3$  has  $(x_0, y_0, z_0) = (0.67, 0.29, 0.42)$  kpc (as from their Table 1) and  $\rho_0 = 1.50 \times 10^{10} M_\odot \text{ kpc}^{-3}$ . Figure 23 also shows the mid plane density predicted from the modified Besançon model (shown as black points) and as turquoise points the mid-plane density computed from HI dispersions by Malhotra (1995). The three lines and three sets of points all approximately intersect at a radius between 1.2 and 1.5 kpc. This radius is consistent with the radius estimated for the outer part of the X-shape from red-clump stars by McWilliam & Zoccali (2010) (see their Figure 6). The rotation curve, bar pattern speed, bulge density profile, X-shape size scale and resonance location are all consistent with one another.

The location of the  $\rho_{LR}$  curves shown in Figure 23 are insensitive to the assumed bar pattern speed. We find that varying the bar pattern speed by 5% does not significantly move the curve (see the narrow green line in Figure 23). Because the relation for  $\rho_{LR}$  depends on derivatives of the potential, this function is extremely sensitive to the type of curve fit to the rotation curve data points and the noise and range of these points. This is illustrated by the difference between the density curves  $\rho_{LR,m}$  and  $\rho_{LR,s}$  that use two different rotation curves to generate  $\Omega$  and  $\kappa$ . The rotation curve by Malhotra (1995) does not extend within 2 kpc so is purely an extrapolation within this radius. The mid-plane

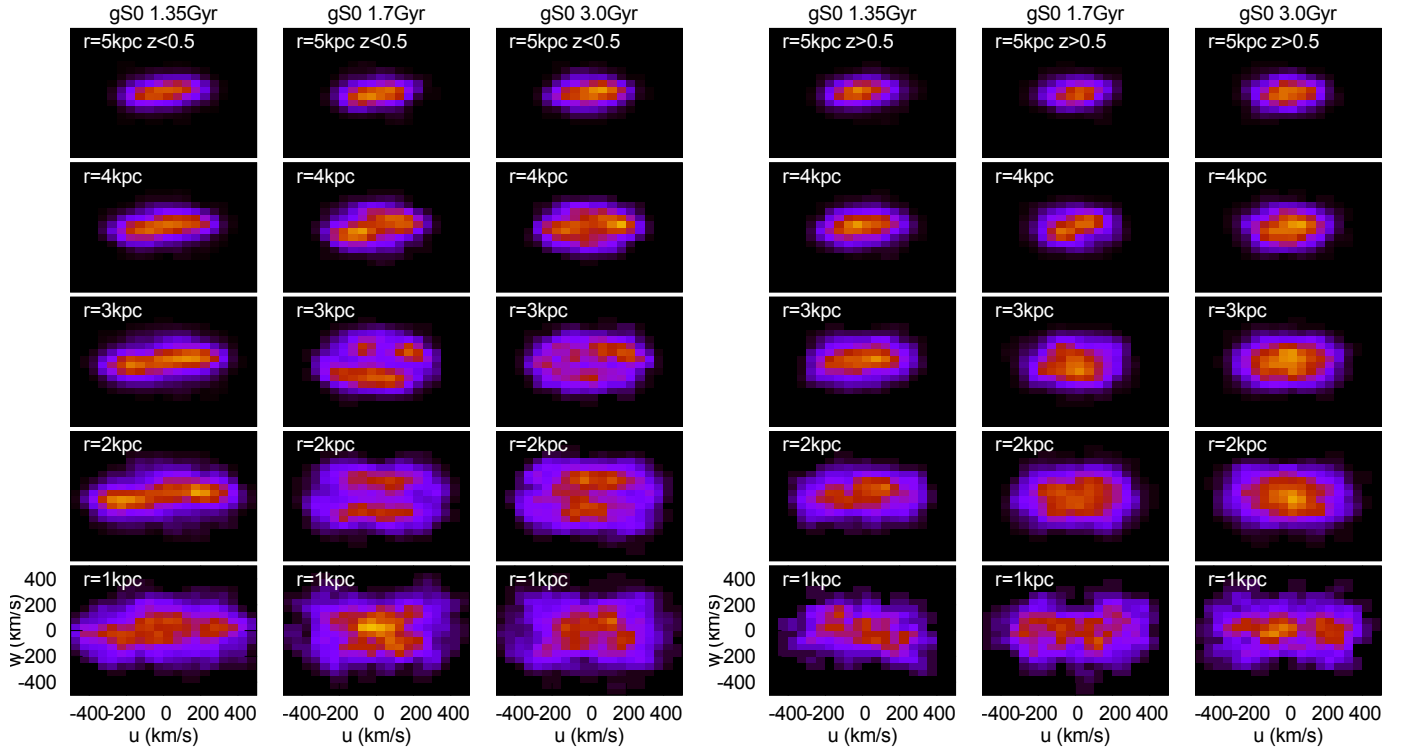


**Figure 20.** Radial ( $u$ ) vs vertical ( $w$ ) velocity distributions generated from snapshots of the gS0 simulation. Similar to Figure 19 except for the gS0 simulation and at times 1.35, 1.7 and 3.0 Gyr. Within the vertical resonance, there are no orbits that remain in the mid-plane. This gives a donut or double bar shape in the mid-plane velocity distributions for radii within the peanut-shape at later times.

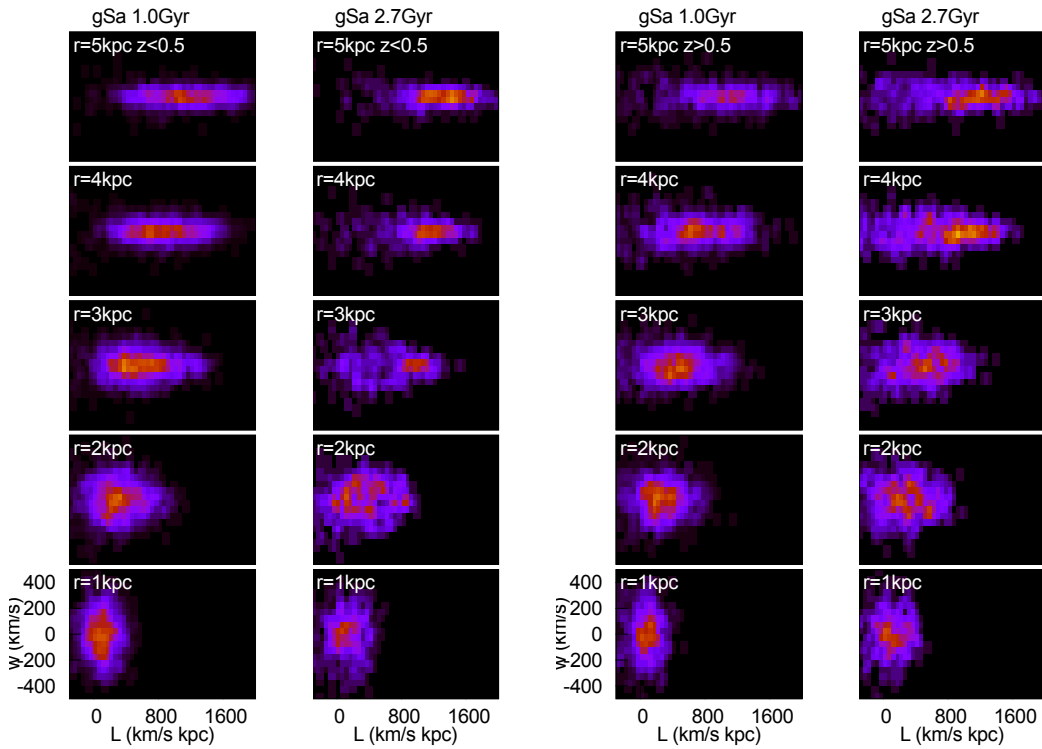


**Figure 21.** Angular momentum vs vertical ( $w$ ) velocity distributions of disk stars from snapshots of the gSa simulation. Similar to Figure 19 except the  $x$ -axis corresponds to angular momentum. Within an angular momentum value associated with the vertical resonance, 1000 km/s kpc, the vertical velocity dispersion is wide. Outside this angular momentum value, the vertical velocity distribution is narrow.

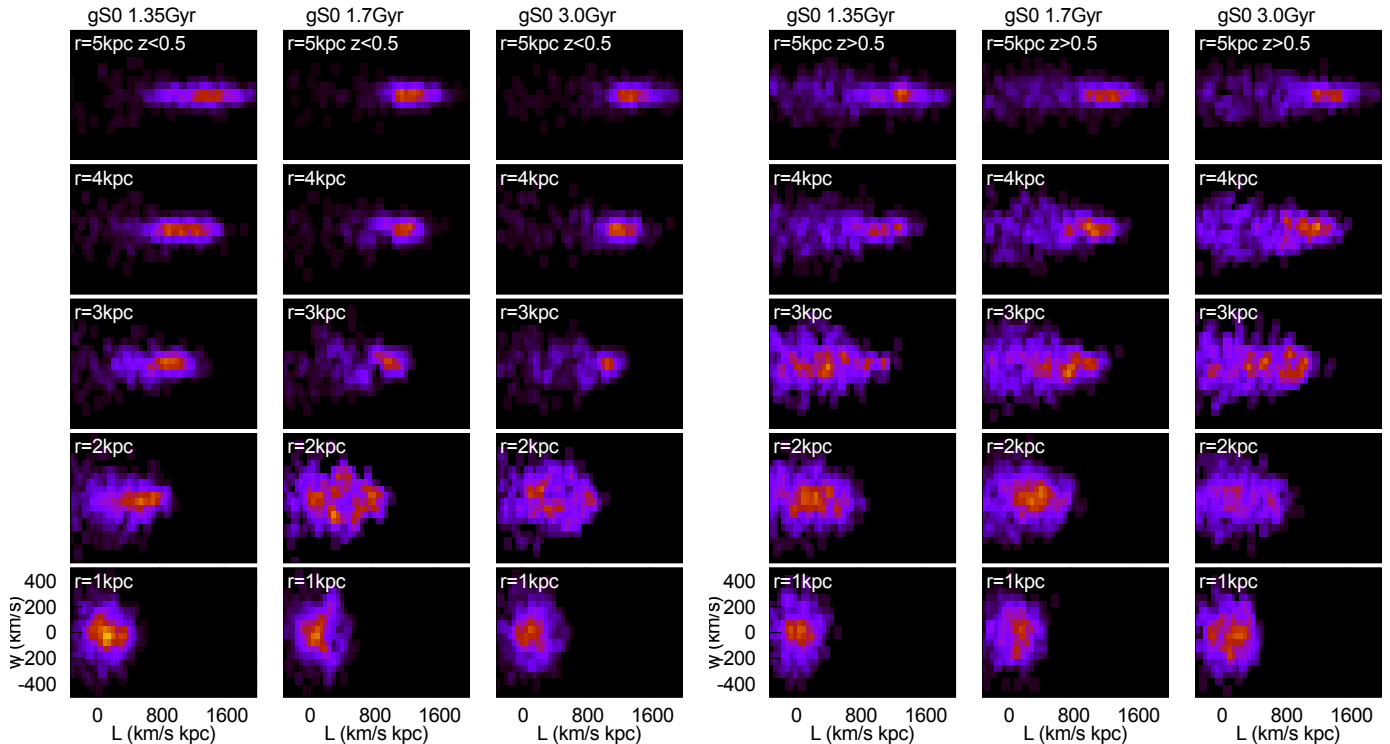


**Figure 22.** Angular momentum vs vertical velocity distributions from snapshots of the gS0 simulation. Similar to Figure 21 except for the gS0 simulation.

density  $\rho_{HI}$  estimated from HI dispersions is extrapolated from radius  $r > 2$  kpc and so is likely an underestimate for the mid-plane density within the bulge. The bulge mid plane profile based on models by Cao et al. (2013) is somewhat high compared to the entire mid plane density (include disk and halo components) predicted by the Besançon model. The Hamiltonian model we discuss here does not take into account the radial degree of freedom, however the orbits in the X are likely to be eccentric. To make better constraints on the mass distribution from the observed distribution of the orbits supporting the X-shape, the orbital eccentricity must be understood and taken into account.

## 5 SUMMARY AND DISCUSSION

We have explored a Hamiltonian resonance model for X-shaped or peanut-shaped galactic bulges. By computing the vertical oscillation frequency from the gravitational potential in N-body simulations, we confirm that the X- or peanut-shape is located near the 2:1 vertical resonance with the bar, which is associated with upward and downwards facing periodic banana-shaped orbits. This confirms previous studies that computed periodic orbit families and attributed the peanut-shape to stars in banana-shaped periodic orbits. (e.g., Combes et al. 1990; Patsis 2002; Martinez-Valpuesta et al. 2006). Here the banana shaped orbits arise in the Hamiltonian model as fixed points that correspond to high inclination orbits in or near resonance. They are associated with orbits that have an angle  $\phi$ , librating about 0 or  $\pi$ , that de-

pends on azimuthal angle  $\theta$  and the angle associated with vertical oscillations  $\theta_z$ .

We examine two simulations, one contains a bar that buckles, the other exhibits a peanut-shaped bulge even though the bar does not buckle. In the bar-buckling simulation, as the bulge thickens during buckling, the vertical oscillation frequency decreases and so the resonance and peanut-shape moves to larger radius. In the buckle-free simulation, the resonance and the peanut-shape moves outward as the bar slows down. In both cases, the location of the peanut shape is consistent with the location of the resonance computed from the current mass distribution. The Hamiltonian model predicts a narrow resonance width in angular momentum distance from commensurability of  $dL/L \sim 0.05$  kpc, a region where there are no planar orbits. As the bar slows down and disk thickens, the resonance moves outwards heating the disk. Stars in the mid plane, just outside resonance, are pushed to high inclination when they encounter the resonance. They reside just inside the resonance separatrix and support the peanut shape until the separatrix shrinks leaving them at high inclination but no longer supporting or moving with the peanut shape. The peanut height predicted from the Hamiltonian model, using the separatrix height and coefficients measured from the simulations, is approximately consistent with that seen in the simulations. Using the libration frequency predicted from the Hamiltonian model, we compare the drift rate to that defining the adiabatic limit and find that the drift rate is comparable to the adiabatic limit. This implies that stars are in resonance, just long enough to be lifted by it.

We interpret the X-shape as primarily due to the popu-

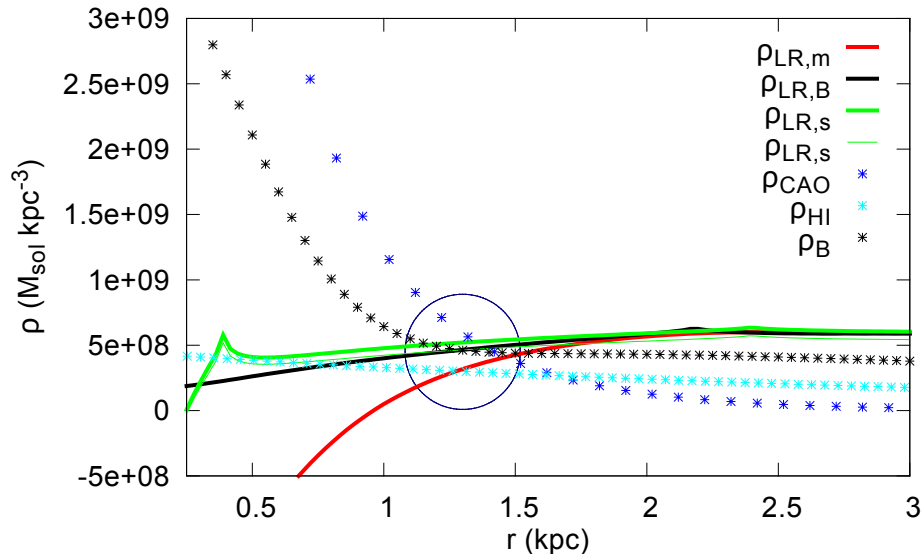


**Figure 23.** Constraints on the Milky Way bulge. The lines show the mid-plane density,  $\rho_{LR}(r)$ , as a function of radius, with density function given in equation 31, computed using Poisson’s equation, the 2:1 vertical resonance condition, and the bar pattern speed estimated by Gardner & Flynn (2010); Minchev et al. (2007). The red line ( $\rho_{LR,m}$ ), and green line ( $\rho_{LR,s}$ ), computes this density using a rotation curve by Malhotra (1995) and by Sofue (2012), respectively. The black lines is similarly computed except using the rotation curve predicted from a Besançon model. The black points show the mid plane density,  $\rho_B$ , for the Besançon model. The blue points show the mid plane density,  $\rho_{CAO}$ , for the azimuthally averaged bulge E3 model by Cao et al. (2013). The turquoise points show the mid-plane density estimated by Malhotra (1995) from the velocity dispersion in HI. The region of intersection of the lines and points, shown with the navy circle, implies that the mid-plane density is  $5 \pm 1 \times 10^8 M_{\odot} \text{kpc}^{-3}$  at a radius of  $1.4 \pm 0.2$  kpc and that this radius is the location of the vertical resonance. As the lines and points approximately intersect, the rotation curve, bar pattern speed, mid-plane density and bulge density profiles are all nearly consistent with one another. The narrow green line shows the small effect of lowering the bar pattern speed by 5%. A comparison between the red, green and black lines show the sensitivity to uncertainties in the rotation curve. The peak in the green curve at small radii is an artifact caused by a drop in the rotation velocity at very smaller radius and the low order of polynomial used to fit the rotation curve.

lation of stars that is supporting the peanut shape that have just recently been excited by the resonance as the resonance drifts outward. Stars within the resonance separatrix would either be upwards banana shaped or downwards banana-shaped orbits. Those recently escaping resonance, and just outside the resonance separatrix, would have morphology similar to a sum of upwards and downwards banana-shaped orbits and spend more time aligned with the bar and so support the peanut shape. After stars leave resonance they no longer support the peanut shape and so don’t maintain a coherent vertical feature that is aligned with the bar. Stars supporting the X-shape would primarily be disk stars, the latest ones captured into resonance that were in the mid plane prior to their capture into resonance. As they were all disk stars they should have similar metallicity and that typical of the disk just exterior to resonance.

Velocity distributions along the bar major axis in numerical simulations show that there are no stars in orbits in the mid-plane within the vertical resonance, as expected from a drifting Hamiltonian model. The distribution of angular momentum versus vertical velocity shows that stars below a certain angular momentum value associated with resonance exhibit a much larger vertical velocity dispersion than stars outside resonance. The velocity distributions are wide, suggesting that as the resonance is swept through the disk, stars are heated by it. Division into bulge and disk might be made based on the angular momentum value as-

sociated with the vertical resonance as stars are pushed out of the plane via passage through the resonance.

We previously proposed that peanut shaped bulges arose from resonance capture during bar growth (Quillen 2002) and that the X-shape arose from the height of periodic orbits as a function from distance from resonance. Here we find that that the resonance width is too narrow to account for the X-shape. Instead the resonance is swept through the disk due to slowing of the bar and thickening of the disk. Because of the narrow width of the resonance, only orbits in the vicinity of the resonance can exhibit vertical structure coherent with the bar. Consequently stars recently captured into resonance or near the resonance separatrix are responsible for the X-shape. The X-shape can be attributed to the orbital shapes of this resonant population of stars. If the resonance has drifted outward, these stars lie in the vicinity of the resonance separatrix at the outer boundary of the resonance. Stars within the separatrix are not near periodic orbits but do exhibit angles  $\phi$  that librate about 0 or  $\pi$ . Those outside the separatrix exhibit oscillating  $\phi$  but spend more time with  $\phi$  near 0,  $\pi$  than near  $\pm\pi/2$ .

The low order Hamiltonian model provides a promising predictive dynamical framework to describe features of peanut-shaped bulges, and relate orbital properties to the bar strength, pattern speed and vertical oscillation frequency. Time dependent models were only qualitatively explored here, however with additional calculation they may be able to predict velocity distributions, relate the cur-

rent distributions to past evolution and reconcile the differences in theoretical framework between the vertical resonance model and the bar buckling instability model for peanut formation.

An estimate of the mid-plane mass density can be made in the bulge of the Milky Way at the location of the resonance. We find that the mid-plane density is approximately  $5 \times 10^8 M_{\odot} \text{kpc}^{-3}$  at a radius of 1.3 kpc and that this is approximately the location of the vertical resonance and recently discovered X-shape (Nataf et al. 2010; McWilliam & Zoccali 2010). This density is approximately consistent with the axisymmetric average at the same radius of the E3 bulge mode by Cao et al. (2013) and that of the Besançon model. Thus the rotation curve, vertical resonance location, X-shape tips, and mid plane mass density, are all self-consistent in the Milky Way galaxy bulge.

The largest uncertainty in estimating the location of the resonance is due to errors in the rotation curve in the bulge, that are exacerbated when taking derivatives. We identify the resonance location as a function of angular momentum. However the orbits supporting the X-shape are likely to have eccentricity similar to stars just outside the vertical resonance. That implies that these stars would be located at larger galactocentric radius near the ends of the bar than along the bar minor axis. We have neglected the mean ellipticity of orbits in our computation. To improve upon constraint based on the resonance location, the ellipticity of the orbits must be taken into account. The extreme sensitivity of the vertical resonance model to rotation curve, bar shape, strength and pattern speed, and disk thickness, imply that future work will make it possible to place tight constraints on the structure and evolution of the Milky Way disk and bulge.

We explored here numerical simulations with live halos and with bars that decreased in pattern speed. We have focused on the setting with resonance moving outward either due to disk thickening or bar slowing. Future studies can also study simulations (such as that by Li & Shen 2012) that have steadier bars. If the bar speeds up then the interpretation would change dramatically as in this case stars can be captured into periodic orbits and lifted while remaining in resonance. The Hamiltonian model has been improved and corrected in appendices A and B, however it does not take into account the radial degree of freedom. Future work is required to predict the three dimensional structure of orbits supporting the X- or peanut-shape.

This work was in part supported by NASA grant NNX13AI27G and a travel grant from the IAU. We thank Nanjing University and Shanghai Observatory for their generous and gracious hosting June 2013. We thank David Nataf, Liang Cao, Juntai Shen, and Victor Debattista for helpful comments and communications.

## REFERENCES

Athanassoula, E. 2005, *MNRAS*, 358, 1477  
 Bovy, J. et al. 2012, *ApJ*, 759, 131

Bureau, M., Aronica, G., Athanassoula, E., Dettmar, R.-J., Bosma, A., & Freeman, K. C. 2006, *MNRAS*, 370, 753  
 Cao, L., Mao, S., Nataf, D., Rattenbury, N. J. & Gould, A. 2013, in press, arXiv:1303.6430  
 Combes, F., & Sanders, R. H. 1981, *A&A*, 96, 164  
 Combes F., Debbasch F., Friedli D., & Pfenninger D., 1990, *A&A*, 233, 82  
 Contopoulos, G. 1975, *ApJ*, 201, 566  
 Debattista, V. P., Carollo, C. M., Mayer, L. & Moore, B. 2005, *ApJ*, 628, 678  
 Di Matteo, P., Combes, F., Melchior, A.-L., and Semelin, B. 2007, *A&A* 468, 61  
 Dwek, E., Arendt, R. G., Hauser, M. G., Kelsall, T., Lisse, C. M., Moseley, S. H., Silverberg, R. F., Sodroski, T. J., & Weiland, J. L. 1995, *ApJ*, 445, 716  
 Erwin, P., & Debattista, V. P. 2013, *MNRAS*, 431, 3060  
 Gardner, E., Debattista, V. P., Robin, A. C., Vasquez, S., & Zoccali, M. *MNRAS*, 2013, in press, arXiv:1306.4694  
 Gardner, E., & Flynn, C., 2010, *MNRAS*, 405, 545, also 2010, *MNRAS*, 406, 701  
 Gardner, E., & Flynn, C. 2010, *MNRAS*, 406, 701  
 Chilingarian, I., Di Matteo, P., Combes, F., Melchior, A.-L., & Semelin, B. 2010, *A&A*, 518, 61  
 Friedli, D. & Pfenninger, D. 1990, in *ESO/CTIO Workshop on Bulges of Galaxies*, ed. B. Jarvis & D. M. Terndrup (Garching: ESO), 265  
 Gerhard, G. & Martinez-Valpuesta, I. 2012, *ApJL*, 744, L8  
 Heisler, J., Merritt, D., & Schwarzschild, M. 1982, *ApJ*, 258, 490  
 Laurikainen, E., Salo, H., Buta, R., & Vasylyev, S. 2004, *MNRAS*, 355, 1251  
 Li, Z.-Y., & Shen, J. 2012, *ApJ*, 757, L7  
 Lütticke, R., Dettmar, R.-J., Pohlen, M. 2000, *A&A*, 362, 435  
 Malhotra, S. 1995, *ApJ*, 448, 138  
 Martinez-Valpuesta, I., Shlosman, I., & Heller, C. 2006, *ApJ*, 637, 214  
 McWilliam, A., & Zoccali, M. 2010, *ApJ*, 724, 1491-1502  
 Mendez-Abreu, J., Corsini, E. M., Debattista, V. P., De Rijcke, S., Aguerri, J. A. L., & Pizzella, A. 2008, *ApJ*, 679, L73  
 Merritt, D. & Sellwood, J. A. 1994, *ApJ*, 425, 551  
 Minchev, I., Nordhaus, J., & Quillen, A. C. 2007, *ApJ*, 664, L31  
 Minchev, I., Famaey, B., Quillen, A. C., Di Matteo, P., Combes, F., Vlahic, M., Erwin, P., & Bland-Hawthorn, J. 2012, *A&A*, 548, 126  
 Murray, C. D., & Dermott, S. F. 1999, *Solar System Dynamics* (Cambridge: Cambridge Univ. Press)  
 Nataf, D. M., Udalski, A., Gould, A. Fouque, P., & Stanek, K. Z. 2010, *ApJ*, 721, L28  
 Ness, M., Freeman, K., Athanassoula, E., Wylie-De-Boer, E., Bland-Hawthorn, J., Lewis, G. F., Yong, D., Asplund, M., Lane, R. R., Kiss, L. L., Ibata, R. 2012, *ApJ*, 756, 22  
 Patsis, P. A., Skokos, C., & Athanassoula, E. 2002, *MNRAS*, 337, 578  
 Pfenninger, D., & Friedli, D. 1991, *A&A*, 252, 75  
 Poleski, R., Udalski, A., Gould, A., Szymanski, M. K., Soszynski, I., Kubiak, M., Pietrzynski, G., Ulaczyk, K., & Wyrzykowski, L. 2013, *ApJ* in press, arXiv1304.6084  
 Quillen, A. C. 2002, *AJ*, 124, 722  
 Quillen, A. C. 2006, *MNRAS*, 365, 1367

- Raha, N., Sellwood, J. A., James, R. A., & Kahn, F. D. 1991, *Nature*, 352, 411
- Robin, A. C., Reyle, C., Derriere, S., & Picaud, S. 2003, *A&A* 409, 523-540
- Saito, R. K., Zoccali, M., McWilliam, A., Minniti, D., Gonzalez, O. A., & Hill, V. 2011, *AJ*, 142, 76
- Skokos, Ch., Patsis, P. A., & Athanassoula, E. 2002, *MNRAS*, 333, 847
- Sofue, Y. 2012, *PASJ*, 64, 75
- Sridhar, S., & Touma, J. 1996, *MNRAS*, 279, 1263
- Sridhar, S., & Touma, J. 1996, *Science*, 271, 973
- Vásquez, S., Zoccali, M., Hill, V., Renzini, A., González, O. A., Gardner, E., Debattista, V. P., Robin, A. C., Rejkuba, M., Baffico, M., Monelli, M., Motta, V., & Minniti, D. 2013, *A&A*, in press, *astroph-1304.6427*

## APPENDIX A: ACTION ANGLE VARIABLES FOR AN AXISYMMETRIC GALAXY TO LOW ORDER IN EPICYCLIC AMPLITUDE AND VERTICAL OSCILLATION AMPLITUDE

In this section we review the extension of a low order Hamiltonian theory to cover vertical oscillations in a galactic disk. We extend and correct the previous calculation by Quillen (2002). The Hamiltonian is expanded to low order in epicyclic and vertical action variables. Rather than expand in angular momentum (as done by Contopoulos 1975) we use coefficients that are functions of the angular momentum and we retain the angular momentum as an action variable.

The dynamics of a massless particle in a galaxy with an axisymmetric gravitational potential,  $V_0(r, z)$ , can be described with the Hamiltonian

$$H_0(r, z, \theta; p_r, p_z, L) = \frac{L^2}{2r^2} + \frac{p_r^2}{2} + \frac{p_z^2}{2} + V_0(r, z) \quad (\text{A1})$$

where  $r, z, \theta$  are cylindrical coordinates and  $p_r, p_z, L$  are associated momenta. We can transform to new momenta and coordinates  $(\theta_r, \theta_z, \theta_{new}; J_r, J_z, L_{new})$  with a generating function that depends on old momenta  $(p_r, p_z, L)$  and new coordinates  $(\theta_r, \theta_z, \theta_{new})$

$$F_3(p_r, p_z, L; \theta_r, \theta_z, \theta_{new}) = \frac{p_r^2}{2\kappa(L)} \cot \theta_r + \frac{p_z^2}{2\nu(L)} \cot \theta_z - r_c(L)p_r - L\theta_{new} \quad (\text{A2})$$

giving a canonical transformation that relates old coordinates and momenta to new ones

$$\begin{aligned} r &= r_c(L) + \sqrt{\frac{2J_r}{\kappa(L)}} \cos \theta_r \\ p_r &= -\sqrt{2J_r\kappa(L)} \sin \theta_r \\ z &= \sqrt{\frac{2J_z}{\nu(L)}} \cos \theta_z \\ p_z &= -\sqrt{2J_z\nu(L)} \sin \theta_z \\ \theta &= \theta_{new} - r'_c(L)\sqrt{2J_r\kappa} \sin \theta_r \\ &\quad + \frac{\kappa'(L)J_r}{2\kappa} \sin(2\theta_r) + \frac{\nu'(L)J_z}{2\nu} \sin(2\theta_z) \\ L &= L_{new}, \end{aligned} \quad (\text{A3})$$

where  $r'_c(L) = \frac{\partial r_c(L)}{\partial L}$  and similarly for  $\kappa'(L)$  and  $\nu'(L)$ . Hereafter we do not make a distinction between  $L$  and  $L_{new}$  or  $\theta$  and  $\theta_{new}$ . The radius of a particle with angular momentum  $L$  in a circular orbit is  $r_c(L)$  and

$$L^2 = r_c^3(L) \left. \frac{\partial V_0}{\partial r} \right|_{r=r_c(L), z=0} \quad (\text{A4})$$

or

$$r_c(L) = \sqrt{\frac{L}{\Omega(L)}}. \quad (\text{A5})$$

with  $\Omega(L)$  the angular rotation rate of a particle in a circular orbit in the mid-plane with angular momentum  $L$ . The epicyclic frequency,  $\kappa(L)$ , satisfies

$$\kappa^2(L) = 3\Omega^2(L) + \left. \frac{\partial^2 V_0}{\partial r^2} \right|_{r=r_c(L), z=0} \quad (\text{A6})$$

and it may be convenient to recall

$$\Omega^2(L) = \frac{1}{r_c(L)} \left. \frac{\partial V_0}{\partial r} \right|_{r=r_c(L), z=0}. \quad (\text{A7})$$

The vertical oscillation frequency,  $\nu(L)$  satisfies

$$\nu^2(L) = \left. \frac{\partial^2 V_0}{\partial z^2} \right|_{r=r_c(L), z=0} \quad (\text{A8})$$

The derivatives with respect to  $L$

$$\begin{aligned} r'_c(L) &= \frac{\partial r_c(L)}{\partial L} = \frac{2L}{r_c(L)^3 \kappa(L)^2} = \frac{2\Omega(L)}{\kappa(L)} \frac{1}{r_c(L)\kappa(L)} \\ \Omega'(L) &= \frac{1}{r_c^2} \left[ 1 - \frac{4\Omega^2}{\kappa^2} \right] \\ \kappa'(L) &= \frac{L}{r_c^3 \kappa^3} \left[ \frac{\partial^3 V_0}{\partial r^3} + \frac{3}{r_c} \frac{\partial^2 V_0}{\partial r} - \frac{3}{r_c^2} \frac{\partial V_0}{\partial r} \right]_{r_c(L), z=0} \\ &= \frac{L}{r_c^3 \kappa^3} \left. \frac{\partial \kappa^2}{\partial r} \right|_{r=r_c(L), z=0} \\ \nu'(L) &= \frac{L}{r_c^3 \kappa^2 \nu} \left. \frac{\partial^3 V_0}{\partial r \partial z^2} \right|_{r=r_c(L), z=0} \end{aligned} \quad (\text{A9})$$

Here  $\kappa'(L)$  is related to the  $\lambda_0$  parameter used by Contopoulos (1975) (see his equation A10).

The variables  $J_r$  and  $\theta_r$  are the epicyclic action and angle and  $J_z$  and  $\theta_z$  are the action and angle for vertical oscillations. It is sometimes convenient to discuss an epicyclic amplitude,  $\sqrt{2J_r/\kappa}$ , or vertical oscillation amplitude,  $\sqrt{2J_z/\nu}$ . The amplitudes can be described in terms of an orbital eccentricity,  $e = \frac{1}{r_c} \sqrt{\frac{2J_r}{\kappa}}$ , or an orbital inclination,  $i = \frac{1}{r_c} \sqrt{\frac{2J_z}{\nu}}$ .

The new Hamiltonian in the new coordinate system, expanded to fourth order in  $J_z^{1/2}$  and  $J_r^{1/2}$ , and assuming that  $V$  is symmetric about the mid-plane, is

$$\begin{aligned} H_0(\theta_r, \theta_z, \theta; J_r, J_z, L) &= \frac{L^2}{2r_c^2} + V(r_c) + \kappa J_r + \nu J_z \\ &\quad + \left( \frac{2J_r}{\kappa} \right)^{\frac{3}{2}} \cos^3 \theta_r \left( -\frac{4L^2}{2r_c^5} + \frac{1}{6} \left. \frac{\partial^3 V_0}{\partial r^3} \right|_{r=r_c, z=0} \right) \\ &\quad + \left( \frac{2J_r}{\kappa} \right)^2 \cos^4 \theta_r \left( \frac{5L^2}{2r_c^6} + \frac{1}{24} \left. \frac{\partial^4 V_0}{\partial r^4} \right|_{r=r_c, z=0} \right) \end{aligned}$$

$$\begin{aligned}
& + \left( \frac{2J_r}{\kappa} \right)^{\frac{1}{2}} \left( \frac{2J_z}{\nu} \right) \cos \theta_r \cos^2 \theta_z \frac{1}{2} \frac{\partial^3 V_0}{\partial r \partial z^2} \Bigg|_{r=r_c, z=0} \\
& + \left( \frac{2J_r}{\kappa} \right) \left( \frac{2J_z}{\nu} \right) \cos^2 \theta_r \cos^2 \theta_z \frac{1}{4} \frac{\partial^4 V_0}{\partial^2 r \partial^2 z} \Bigg|_{r=r_c, z=0} \\
& + \left( \frac{2J_z}{\nu} \right)^2 \cos^4 \theta_z \frac{1}{24} \frac{\partial^4 V_0}{\partial z^4} \Bigg|_{r=r_c, z=0} \quad (A10)
\end{aligned}$$

and our choice for functions  $r_c(L), \kappa(L), \nu(L)$  has cancelled some low order terms.

It is useful to keep in mind the trigonometric identities

$$\begin{aligned}
\cos^3 \phi &= \frac{1}{4} \cos 3\phi + \frac{3}{4} \cos \phi \\
\cos^4 \phi &= \frac{1}{8} \cos 4\phi + \frac{1}{2} \cos 2\phi + \frac{3}{8} \\
\cos^2 \phi_a \cos^2 \phi_b &= \frac{1}{4} [\cos(2(\phi_a + \phi_b)) + \cos(2(\phi_a - \phi_b))] \\
&+ \frac{1}{2} [\cos(2\phi_a) + \cos(2\phi_b) + 1] \quad (A11)
\end{aligned}$$

We can remove terms proportional to cosine functions of  $\theta_z$  or  $\theta_r$  by performing canonical transformations that include terms that are dependent on the Fourier components such as  $\cos m\theta_r$ , or  $\cos m\theta_r$  with  $m = 1, 2, 3, 4$ , as illustrated in the appendix by Quillen (2002). This can be done as long as the time derivative of the angles are not small (there are no small divisors). The constant coefficients in the expansion of  $\cos^4 \theta_r$  and  $\cos^4 \theta_z$  give terms proportional to  $J_r^2$  and  $J_z^2$ . The term with  $\cos^2 \theta_r \cos^2 \theta_z$  gives a term proportional to  $J_r J_z$ . With respect to the perturbed coordinates and momenta

$$H_0(\theta_r, \theta_z, \theta_{new}; J_r, J_z, L) = g_0(L) + \kappa(L)J_r + \nu(L)J_z \quad (A12) \\
+ a_z(L)J_z^2 + a_r(L)J_r^2 + a_{rz}(L)J_z J_r$$

with

$$\begin{aligned}
g_0(L) &= \frac{L^2}{2r_c^2} + V(r_c) \\
a_z(L) &= \frac{4}{\nu^2} \frac{3}{8} \frac{1}{4!} \frac{\partial^4 V_0}{\partial z^4} \Bigg|_{r=r_c, z=0} = \frac{1}{16\nu^2} \frac{\partial^4 V_0}{\partial z^4} \Bigg|_{r=r_c, z=0} \\
a_r(L) &= \frac{4}{\kappa^2} \frac{3}{8} \left( \frac{5L^2}{2r_c^4} + \frac{1}{24} \frac{\partial^4 V_0}{\partial r^4} \Bigg|_{r=r_c, z=0} \right) \\
&= \frac{15L^2}{4r_c^4 \kappa^2} + \frac{1}{16\kappa^2} \frac{\partial^4 V_0}{\partial r^4} \Bigg|_{r=r_c, z=0} \\
a_{rz}(L) &= \frac{1}{4\nu\kappa} \frac{\partial^4 V_0}{\partial^2 r \partial^2 z} \Bigg|_{r=r_c, z=0} \quad (A13)
\end{aligned}$$

We correct by a factor of 2 the expression for  $a_z$  from that given in equation 7 and 16 by Quillen (2002). The zeroth order function  $g_0(L)$  is such that  $\frac{\partial g_0(L)}{\partial L} = \Omega(L)$ , as expected. The last coefficient can also be written

$$a_{rz}(L) = \frac{1}{4\nu\kappa} \frac{\partial^2 \nu^2}{\partial r^2} \Bigg|_{r=r_c, z=0} \quad (A14)$$

correcting the coefficient of the last term in equation 7 by Quillen (2002) that has incorrect units.

The expression for  $a_r(L)$  above differs from the coefficient given in equation A32 by Contopoulos (1975). Here we have expanded to low orders in  $J_r^{1/2}$  and  $J_z^{1/2}$  and not expanded about a particular  $L$  value. In other words the Hamiltonian in equation A12 contains low orders of  $J_r, J_z$

but the coefficient for each term is a function of  $L$ . Contopoulos (1975) does not use functions of angular momentum but expands about a value for  $L$  corresponding to a particle in a circular orbit at a particular energy value.

It is convenient to transform to a frame that rotates with the bar so that the new Hamiltonian is conserved. Using a generating function  $F_2(\theta_{new}, L') = (\theta_{new} - \Omega_b t)L'$  we transfer to a frame rotating with the bar finding new azimuthal angle in the corotating frame

$$\theta_{cr} = \theta_{new} - \Omega_b t$$

and angular momentum unchanged  $L = L'$  so we drop the prime, and new Hamiltonian

$$K_0(\theta_r, \theta_z, \theta_{cr}; J_r, J_z, L) = g_0(L) - \Omega_b L + \kappa(L)J_r \quad (A15) \\
+ \nu(L)J_z + a_z(L)J_z^2 + a_r(L)J_r^2 + a_{rz}(L)J_z J_r$$

With the addition of a bar perturbation,  $V_b$ , that is time independent in the frame rotating with the bar, the Hamiltonian is  $K = K_0 + V_b$  and is time independent, so  $K$  is a conserved quantity that is called the Jacobi integral of motion or the Jacobi constant. Here  $V_b$  is the sum of the Fourier components (equation 7) and has an azimuthal average of zero.

## APPENDIX B: CANONICAL TRANSFORMATION TO A LOW DIMENSIONAL HAMILTONIAN

We perform a canonical transformation so that  $\phi = \theta_z - \frac{m}{2}\theta_{cr} = \theta_z - \frac{m}{2}(\theta - \Omega_b t)$  becomes a canonical coordinate. We use a generating function in terms of new momenta ( $J'_z, J'_r, I$ ) and old coordinates ( $\theta_z, \theta_r, \theta_{cr}$ )

$$F_2(J'_z, J'_r, I; \theta_z, \theta_r, \theta_{cr}) = \left( \theta_z - \frac{m}{2}\theta_{cr} \right) J'_z + J'_r \theta_r + I \theta_{cr} \quad (B1)$$

giving new momenta and coordinates in terms of old ones

$$I = \frac{m}{2} J_z + L \quad (B2)$$

$$\phi = \theta_z - \frac{m}{2}\theta_{cr} \quad (B3)$$

Momenta  $J'_z = J_z$  and  $J'_r = J_r$ , so hereafter we drop the primes. Coordinates  $\theta$  and  $\theta_r$  also remain unchanged by the transformation. Needed for the transformation is  $\frac{\partial F_2}{\partial t} = \frac{m}{2}\Omega_b J_z$  as it contributes to the Hamiltonian in the new variables. The Hamiltonian (equation A15) in the new coordinates expanded to second order in momenta is

$$K_0(\phi, \theta_r, \theta_{cr}; J_z, J_r, I) = g_0(I) - \Omega_b I + \kappa(I)J_r + \delta(I)J_z + \\
a_r(I)J_r^2 + a_{cz}(I)J_z^2 + a_{crz}(I)J_z J_r \quad (B4)$$

with

$$\delta(I) = \nu(I) - \frac{m}{2}(\Omega(I) - \Omega_b) \quad (B5)$$

$$\begin{aligned}
a_{cz}(I) &= a_z(I) + \frac{m^2}{8} \frac{\partial \Omega}{\partial L} - \frac{m}{2} \frac{\partial \nu}{\partial L} \\
&= \frac{1}{16\nu^2} \frac{\partial V_0^4}{\partial z^4} + \frac{m^2}{8r_c^2} \left[ 1 - \frac{4\Omega^2}{\kappa^2} \right] \\
&\quad - \frac{m}{2} \frac{\Omega}{\nu} \frac{1}{r_c \kappa^2} \frac{\partial \nu^2}{\partial r} \quad (B6)
\end{aligned}$$

$$\begin{aligned}
a_{crz}(I) &= a_{rz}(I) - \frac{m}{2} \frac{\partial \kappa(I)}{\partial L} \\
&= \frac{1}{4\nu\kappa} \frac{\partial^4 V_0}{\partial^2 r \partial^2 z} - \frac{m}{2} \frac{\Omega}{r_c \kappa^3} \frac{\partial \kappa^2}{\partial r}
\end{aligned} \tag{B7}$$

where we have used equations A9 for derivatives with respect to  $L$ .

With the addition of a perturbation that depends only on  $\phi$ , the momentum  $I$  (equation B2) is conserved. Ignoring the epicyclic variations, the Hamiltonian is reduced to a single dimension and becomes that given in equation 3 with  $a = a_{cz}$  and  $\delta$  shown above as above. Quillen (2002) did not compute the second and third terms in equation B6 however each of these two terms can dominate the first one. The second and third term have opposite signs, reducing the strength of  $a_{cz}$ .

### APPENDIX C: SHIFT IN RESONANCE LOCATION DUE TO THE $J_R J_Z$ CROSS TERM

The Hamiltonian contains a term proportional to  $J_r J_z$ . As Hamilton's equation  $\dot{\theta}_z = \frac{\partial H}{\partial J_z}$  the  $J_r J_z$  term causes a shift in the frequency  $\dot{\theta}_z$  and so a shift in the location of the vertical resonance. Using the expression for  $J_r = e^2 r_c^2 \kappa / 2$  and eccentricity  $e = \frac{1}{r_c} \sqrt{\frac{2J_r}{\kappa}}$  we can estimate a frequency shift,  $\omega = a_{crz} J_r$ , that depends on eccentricity

$$\delta\omega = \frac{\omega}{\nu} = \frac{a_{crz} J_r}{\nu} = e^2 \left[ \frac{1}{8} \frac{r_c^2}{\nu^2} \frac{\partial^2 \nu^2}{\partial r^2} - \frac{m}{4} \frac{\Omega}{\nu} \frac{r_c}{\kappa^2} \frac{\partial \kappa^2}{\partial r} \right], \tag{C1}$$

using equation B7. Assuming that both  $\kappa$  and  $\nu$  are approximately inversely proportional to  $r$ , we find that the second term dominates and the frequency shift should be positive. Using the approximation  $\kappa \propto r^{-1}$ ,  $\nu \sim 2\Omega$  and for  $m = 4$  we estimate

$$\delta\omega \sim e^2. \tag{C2}$$

For an eccentricity of  $e \sim 0.3$  the frequency shift could be of size 0.1. Because the frequency shift depends on the square of the eccentricity, even within the bar, the shift cannot be large.

When taking into account the  $J_r J_z$  term in the Hamiltonian, the distance to the vertical Lindblad resonance is given by the frequency

$$\delta = \nu(1 + \delta\omega) - 2(\Omega - \Omega_b), \tag{C3}$$

and the resonance is located where

$$\Omega - \frac{\nu}{2} (1 + \delta\omega) \sim \Omega_b. \tag{C4}$$

We expect the shift  $\delta\omega$  to be positive and so it should increase the effect of  $\nu$  in the negative term in the above equation and so would move the resonance slightly inward.

### APPENDIX D: RADIAL DEGREE OF FREEDOM AND ORBITAL ECCENTRICITY

Outside of Lindblad resonances a low order approximation can be used to estimate orbital eccentricity. Neglecting the vertical degree of freedom and to first order in the action

variable  $J_r$ , the unperturbed Hamiltonian (based on equation A15) is

$$K_0(J_r, L; \theta_r, \theta_{cr}) \approx \kappa(L) J_r + g_0(L) - \Omega_b L. \tag{D1}$$

To this we add a perturbation term that is associated with an  $m$ -th Lindblad resonance,  $\epsilon_m J_r^{1/2} \cos(\theta_r - m(\theta - \Omega_b t))$  where  $\epsilon_b$  can be estimated from a bar potential's Fourier components

$$\epsilon_m \approx \sqrt{\frac{2}{\kappa}} \left[ \frac{1}{2} \frac{\partial C_m}{\partial m} + \frac{m\Omega C_m}{r\kappa} \right] \tag{D2}$$

(Contopoulos 1975), where  $C_m$  is the strength of the  $m$ -th Fourier component (equation 7). This gives a total Hamiltonian (in the rotating frame)

$$\begin{aligned}
K_0(J_r, L; \theta_r, \theta_{cr}) &\approx \kappa(L) J_r + g_0(L) - \Omega_b L \\
&\quad + \epsilon_m J_r^{1/2} \cos(\theta_r - m\theta_{cr}).
\end{aligned} \tag{D3}$$

Following a canonical transformation or using Hamilton's equations, we can estimate  $J_r$  at a fixed point

$$J_{r, fixed} = \left( \frac{\epsilon_m}{2\Delta} \right)^2 \tag{D4}$$

where  $\Delta = \kappa - m(\Omega - \Omega_b)$  is the distance to resonance. Taking  $m = 2$ , relevant for the 2:1 Lindblad resonance and using equation D2 for  $\epsilon_2$ , we estimate

$$J_{r, fixed} \approx 2r^2 \Omega \left( \frac{\Omega}{\kappa} \right)^3 \left( \frac{C_2}{r^2 \Omega^2} \right)^2 \left( \frac{\Omega}{\Delta} \right)^2 \tag{D5}$$

Fixed points for  $m = 2$  corresponding to oval periodic orbits in the plane that are aligned with the bar.

We can relate this to the eccentricity of the periodic orbit with  $e = r_c^{-1} \sqrt{2J_{r, fixed} / \kappa}$  giving

$$e_{periodic} = \left( \frac{\Omega}{\kappa} \right)^2 \left( \frac{C_2}{r^2 \Omega^2} \right) \left( \frac{\Omega}{\Delta} \right) \tag{D6}$$

giving a relation between the bar's Fourier components and the eccentricity of periodic orbits. The relation diverges near the Lindblad resonance where  $\Delta \rightarrow 0$ , but this is an artifact of the low order (in  $J_r$ ) of the Hamiltonian model. As long as the Lindblad resonance is not coincident with the vertical Lindblad resonance, the approximation is not divergent. Where  $J_r \neq J_{r, fixed}$  orbits oscillate about  $J_{r, fixed}$ , so  $e_{periodic}$  can be used to estimate the eccentricity of the orbital distribution.